UNIVERSITÀ DEGLI STUDI DI CAGLIARI

DOTTORATO DI RICERCA IN FISICA – XIX CICLO

OPTICAL AND STRUCTURAL CHARACTERIZATION OF CRYSTALLINE OXIDES FOR LASER APPLICATIONS

Docente guida:	Dottorando:
Prof. Alberto Anedda	Daniele Chiriu

Settore Scientifico Disciplinare FIS/01

Contents

Introduction

Although laser operation has been demonstrated in a wide variety of materials, only a very few types of solid-state laser have been developed for research and/or commercial application. In many cases the development of a specific type of laser has been limited due to the lack of availability of high-optical-quality material. This can be due to a number of reasons including the expense of exotic materials and the difficulty in producing large-size synthetic materials with the appropriate properties.

A solid state laser material can be regarded as a physical ensemble of optically active ions dispersed in a host crystal or glass. While operating as an active medium, this material absorbs and emits optical radiation in a controlled thermal environment, and thus its optical spectroscopic properties are critical to its performance. To understand the properties of this system, it is necessary to have extensive knowledge of the physical properties of the free ions, the host material and their interaction mechanism.

This approach implies the study of the electronic states of the optically active ions and the influence of the local electrostatic crystal field of the host and the interactions among active ions.

I.1 Material requirement for Laser Hosts and Active Ions

The choice of a material to be used for solid state laser requires that it must possess suitable chemical, mechanical, thermal, and optical properties. These are determined by a combination of the inherent properties of the host material, the properties of the optically active ions, and the mutual interaction between the host and the dopant ions.

These properties are summarized in the table I.

Host Material

- Rugged and stable with respect to operation environment
- Chemical: stability against thermal, photo, and mechanical changes
- Mechanical
  - High stress-fracture limit
  - Small thermal expansion and stress-optic coefficient to stop lensing
  - High threshold for optical damage
  - Hardness for good polishing
- Optical
  - Minimum scattering centers
  - Minimum parasitic absorption at lasing and pump wavelength
  - Low index of refraction to maximize the stimulated emission cross section

Optically active centers

- Efficient absorption of pump radiation
- Efficient internal conversion to metastable-state population with small quantum defects
- Appropriate energy storage time in the metastable state to utilize all pump energy
- Efficient radiative emission at the laser wavelength with high quantum efficiency
- No absorption at the lasing wavelength (either ground or excited state)
- Emission linewidth compatible with desired tunability and stimulated emission probability
- Ion-ion interaction compatible with maximum pumping and minimum quenching

Total system

- Economic production and fabrication in large size
- Ion-host compatibility
  - Valence and size of substitutional ion similar to host ion
  - Uniform distribution of optical centers in the host

Table I: *Optical properties of active ions and host materials for laser applications.*

In addition, for materials used in closed systems for measurements outside the laboratory, the material should also be rugged and stable with respect to local environmental changes such as temperature, humidity, and stress. Since the operation of the laser requires the exposure of the material to both light and heat, chemical instabilities in the material can be either photo-induced or thermally-induced. Thus, once a material is in use, it must be chemically stable in terms of the valence state of the optically active ions, in terms of ion diffusion, formation of second phases, and formation of color centers and other defects. Last but not least, thermally or optically created internal stress can distort the shape of the material or, in extreme cases, it can causes fractures. Ideal materials have a high stress-fracture limit, small thermal expansion, and small stress-optic coefficient.

The ions useful to providing the optical dynamics of laser materials must be able to efficiently absorb pump radiation and emit at the desired wavelength. Some types of ions have excellent absorption properties but poor emission properties, or vice versa. In this case it is possible to put two types of ions in the same host material, one to absorb the pump energy (called *sensitizer ion*) and the other to provide the laser emission (called *activator ion*). The key to make this system working is to have an efficient non-radiative energy transfer from the sensitizer to the activator. This can be achieved with a strong overlap of the emission spectrum of the sensitizer and the absorption spectrum of the activator. However, if the coupling interaction between the two types of ions is too strong, they no longer have the properties of independent ions, but instead form a coupled ion pair with its own spectral properties.

The optical spectral properties of a laser material are determined by the electronic transitions of the active ions in the local ligand field environment of the host. The types of ions that are useful for laser emission in the near ultraviolet, visible, and near-infrared spectral regions are transition-metal ions and rare-heart ions. These ions have an electron configuration that includes unfilled shells and, as a consequence display electron transitions between energy levels within a specific shell (*d-d* transition for transition metal ions and *f-f* transition for rare-heart ions). These transitions give rise to absorption and emission bands in the desired spectral range. When ions are placed in a host material, the electrostatic interactions with the surrounding ligand ions can split some of the degenerate free-ion energy levels and cause the increase of the probability of some radiative transitions with respect to the others.

I.2 Principal purpose of the study.

Recently the research and development of new generation of solid state laser materials and the optimization, in the optical performances, of active media for non conventional applications, has received new attention. The development of new solid-state lasers, especially those operating between 0.9 and 3.0 μm, has renewed general interest in the optical properties of rare-earth ions (Re^{3+}) in crystalline oxides with garnet structure.

At this purpose, the aim of this study concerns the optical and structural characterization of crystalline oxides for laser application, with the prospective of enhancing efficiency and tunability of solid state lasers, and the experimentation of new materials able to meet specific technological purposes.

Among the principal laser active media, the Neodymium-doped Yttrium Aluminum Garnet (Nd:YAG) is one of the most important available laser systems for research and technological applications. Although its optical characteristics are well known, it has gained new general interest in the perspective of enhancing its efficiency by using different transition metals as sensitizer ions. Indeed the optical properties of some co-dopant ions such as Fe^{3+}, Cr^{3+}, Mn^{2+} in active media have been recently investigated. For example, iron ions in Nd:YAG crystals modify the ultraviolet (UV) optical absorption of the host material near the band edge. The introduction of specific co-dopant affects different physical features of the material and its laser efficiency because of co-dopant and activator energy transfer and possible interaction between co-dopant ions and host material (such as electron-phonon coupling). The study of these interactions constitutes a preliminary step in view of the possible role of Fe^{3+} ion as sensitizer element for enhancing the efficiency of solid state laser media, like Nd:YAG.

The renewed interest in Nd:YAG crystals is also related to the development of new laser materials. The remote sensing of the atmosphere with light detection and ranging (LIDAR) or differential absorption lidar (DIAL) techniques requires the use of specific light sources in order to determine the molecular constituent concentrations present in the atmosphere, such as water vapor.

The possibility of tuning the laser emission to investigate the desired molecule easily explains the growing interest in the optical characterization of mixed garnet materials. In this scenery mixed garnet host materials, like $Y_3Al_5O_{12}$ (YAG), $Y_3Sc_2Ga_3O_{12}$ (YSGG), $Gd_3Sc_2Ga_3O_{12}$ (GSGG) and $Y_3Sc_2Al_3O_{12}$ (YSAG), doped with lanthanides play a key role since the so-called compositional tuning can be achieved by changing the relative concentration of the mixed garnets.

The aim of the present work is to investigate the role of sensitizer ions and the physical properties of mixed crystals by studying the optical and structural properties of two different materials with garnet structure: yttrium aluminum garnet ($Y_3Al_5O_{12}$ -YAG) doped with Fe^{3+} ions, and the mixed structure $Y_3Sc_2Ga_3O_{12}$ (YSGG) - $Y_3Al_5O_{12}$ (YAG) doped with Neodymium.

In order to have an effective control of the optical properties of the analyzed crystals, a deeper insight into the growth process is needed. On this basis, part of the study was spent in the growth laboratory of Scientific Materials Europe (SCIMEX s.r.l. – Tortolì - Italy) and lead to the realization of the samples characterized in the present work, within the framework of a full collaboration between the University of Cagliari and the SCIMEX that produces laser crystals starting from the sintering of primary oxide powders.

The following scheme sums up the work performed for this thesis:

- **Chapter 1:** Introduction to the "Crystal Pulling", with the Czochralski method. Principal characteristics of the YAG-YSGG mixed garnet, Nd:YAG and Fe doped YAG, with applications.
- **Chapter 2:** Elements of group theory and the O_h symmetry**.** Vibrational properties of the garnet structure.
- **Chapter 3:** Crystalline field and splitting of the energy levels of rare earth ions in host materials. Properties of the electron-phonon interactions. Sensitized-crystal lasers.
- **Chapter 4:** Experimental results on YAG-YSGG mixed structure.
- **Chapter 5:** Experimental results on the Fe^{3+} doped yttrium aluminum garnet samples.
- **Conclusions:** The main results with the exposure of the principal work outlooks.

CHAPTER 1

Growth method and analyzed samples

1.1 Crystal pulling: The Czochralski method

The analyzed materials were grown by Czochralski method in the growth laboratory of Scientific Materials Europe (SCIMEX s.r.l. – Tortolì - Italy). Pure oxides of starting materials were mixed and pre-sintered under high pressure and melted in iridium crucible. In order to better understand as the Czochralski process influences the quality of the samples, a part of this thesis was spent in Scientific Materials Europe where experimental growth was performed.

1.1.1. Introduction to the crystal pulling

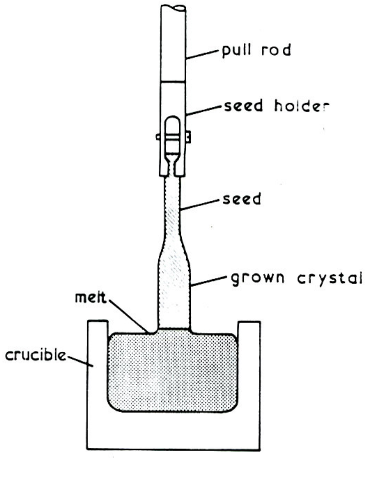

Fig.1.1: *Schematic of crystal pulling*

"Crystal pulling" or the Czochralski method technique (1918) [1,2] is a popular method of crystal growth because it can produce large dislocation-free crystals in a relatively short space of time. The main advantage of the crystal pulling is that it is a "real time" technique whereby the size and diameter of the crystal can be controlled while it is growing. The principle of the method is shown in figure 1.1.

The material to be grown is melted in a crucible. A seed crystal is then dipped into the melt and slowly withdrawn. At the same time the seed is rotated in order to attain thermal symmetry and also to stir the melt. The main requirements for growing good crystals by this method are that the pull and rotation rates should be smooth and that the temperature of the melt should be accurately controlled. The diameter of the crystal is dependent on both the temperature of the melt and the pull rate.

To increase the diameter of a crystal being grown, either the power is reduced or the pull rate decreased, the opposite applies for reducing the diameter. The maximum size of crystal that can be produced by this technique is governed by the volume of the melt, the diameter of the crucible, the distance that the pull rod can move and the strength of the crystal at its minimum diameter.

An additional practical limitation is how well the seed is secured into its holder. If the seed is not secured into its holder it is possible that the crystal detaches and sinks back into the melt.

The choice of the pulling rate is usually a compromise between the crystal growing speed and the generation of defects that this produces [3]. The main cause of defects at high pull rates, particularly with highly doped melts or when growing from solution, is the constitutional supercooling. This phenomenon is important because it indicates the critical temperature gradient that cracks the crystal.

The crystal is rotated in order to avoid a non-circular cross-section which corresponds to the temperature distribution in the melt. If the crucible is not uniformly heated the crystal will grow preferentially towards the coldest region resulting in a non circular cross section.

A slow rotation rate, about 10 rev/min, is sufficient to overcome this occurrence but a higher rotation rate will reduce the impurity build up at the solid-liquid interface. Impurities are often incorporated into the crystal in clusters because of growth rate variations due to temperature fluctuations depending on convective currents in the melt. Impurity content also varies across the diameter of the crystal. The solute rejected close to the peripherical region is rapidly mixed in the large volume of the melt so a higher impurity concentration occurs near the center of the crystal that give rise to a central "core" of impurities. In order to avoid spurious nucleation the melt surface should be free from any kind of particles and the temperature distribution inside the melt should be such that the temperature of solid-liquid interface is the lowest in the liquid.

1.1.2. The melt

The choice of materials and fusion conditions used are very important in order to obtain good quality crystals. Ideally materials should have congruent melting point, low vapor pressure and low viscosity. Crystals should have a suitable growth habit and after solidification no destructive phase changes should occur.

For some materials it is desirable to pull from a non-stoichometric melt or from solution if solvent inclusions arising from constitutional supercooling is avoided. It has been shown by Hurle [4] that constitutional supercooling will be avoided if the following condition holds

$$\frac{K_S G_S - L\rho f}{K_L} \geq \frac{-mfC_L(1-k)}{D[k+(1-k)exp(-\Delta)]}$$

where G_S is the temperature gradient in the solid interface, L is the latent heat of fusion of the solvent, ρ the density, K_S and K_L are the thermal conductivity of solid and liquid respectively, D the diffusion coefficient of solute in the solvent, f is the growth rate. The term Δ is equal to the ratio $f\delta/D$ where δ is the boundary layer thickness and k the distribution coefficient.

1.1.3. Seeding and chamber ambient

The principal advantage of crystal pulling over other techniques of crystal growth is that some defects, eventually present in the seed crystal, do not propagate into the grown crystal. However the ideal seed for crystal pulling is a defect-free, orientated single crystal of the material to be grown [3].

When a crystalline seed is used, some care must be taken in order to be sure that any work damage or residual strain is removed before it is used. A low dislocation seed which has been etched to remove the work-damage layer and annealed to remove strain is preferable. When the seed has been mounted in the crystal puller, it should be lowered slowly towards the melt in order to avoid thermal shock. The melt should be hot enough to melt back some of the seed to ensure that uniform epitaxial growth takes place. The choice of the orientation of the seed can be important in crystal with preferential orientation like $LiNbO_3$, GaAs etc.

The seeding procedure is a critical step in the growth of the crystal. When the temperatures of the seed and of the melt (touch temperature) are not perfectly matched, the formation of stressed zones at the interface and their propagation to the entire crystal are possible [3]. Figure 1.2 displays two YAG crystals obtained with different seeding procedures. In fig. 1.2a the incorrect procedure of touch is shown by the bright regions (stressed zones) while fig. 1.2b shows the correct procedure that avoided the propagation of stress zones in the crystal.

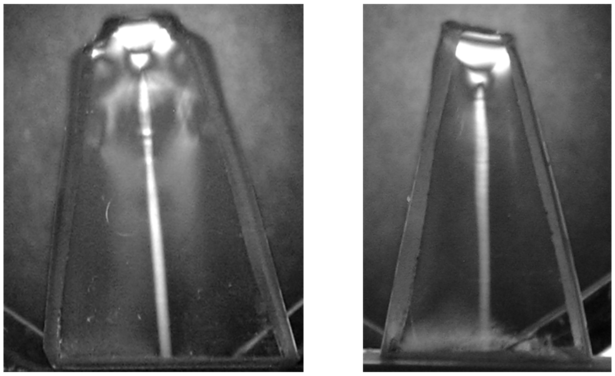

(a) (b)

Fig.1.2: *Different procedure of seeding in YAG crystals. The pictures were obtained by analyzing the light transmission of the samples in crossed polarized conditions.*

The choice of a suitable growing atmosphere is dictated by two principals needs, namely the maintenance of melt stoichiometry and the avoidance of chemical reaction between crystal and/or melt and the surrounding gas [1].

A secondary issue is the thermal conductivity of the gas itself since it affects the crystal temperature distribution during the phase of cooling. The convective heat transport scales with a fractional power of the Grashof number of the flow [3] and, for an ideal gas, this is proportional to the square of the gas pressure. Thus, in high pressure systems, violent convection occurs and convective heat transport can be dominant. When the material to be grown is involatile, vacuum environment provides the cleanest conditions and also allows the continuous removal of potential volatile impurities from the system. In addition any convective heat transport during the growing time is prevented.

1.1.4. The role of hydroxyl impurity (OH^-) during the growth

The knowledge of the impurities incorporated in the crystals and the understanding of their inclusion in the structure are mandatory tasks for monitoring the growth process. There are two types of impurities: desired (generally called crystal dopant) and unwanted (generally referred to as trapped impurities or contaminants) [5]. The impurities are either substitutional (replacing lattice ions) or interstitial (occupying sites between lattice ions) and may alter the structure of the crystal, the distribution of the constituents (either major or minor), the properties of the crystal (optical, electrical, mechanical, etc.), the rates of diffusion of ions or molecules in the crystal surfaces and the growth mechanism.

The presence of impurities or contaminants causes defects in the crystals and their combination with the formation of vacancy point defects in the structure, can largely modify the properties of the crystal. These defects are directly related to the growth process and can be eliminated, or their effects can be minimized, by judicial choice of either the growth procedure or the chemistry of the system (for example lowering or raising the growth temperature etc.) [5].

Among the principal defects in the crystals, related to the growth process, the contaminations of hydroxyl (OH^-) impurities play an important role [6]. In crystalline oxides like $Y_3Al_5O_{12}$, $Y_3Sc_2Al_3O_{12}$, $YAlO_3$ etc. the presence of OH^- can generate color centers and change the optical properties of the crystal. For example the absorption spectra of undoped YAG, where contamination of OH^- and color centers are detected, show the presence of additional bands in UV and IR spectral regions [6]. In addition, when the YAG crystal is used as host material for Nd^{3+} doping, the OH^- impurities localized in the neighborhood of the rare earth can reduce the role of the activator creating “dead sites” [7].

The contamination of OH^- ions in the crystals is ascribed to the growth conditions like residual presence of water vapour or solvents in the chamber, or humidity excess in the prime constituents [1,2].

A careful control of the purity of the constituents and the use of inert gas in the growth chamber, like Argon, can reduce the contamination of hydroxyl ions in the crystals [1-3].

1.1.5. Pull, rotating rates and flux convection

An important parameter governing the quality of a pulled crystal is the flat shape of the solid-liquid interface; a curved interface, in fact, gives rise to a non-uniform impurity distribution across the face of the crystal. The rotation rate is another parameter that affects the shape of the interface and depends by the material to be grown [1]. In addition it alters the flow pattern in the melt and hence the temperature and impurity distribution. Four main types of flow patterns are reported:

1. Thermal convection: this flow consists of a hot stream of liquid lapping on the crucible walls and falling in at the center (*fig. 1.3a*)
2. Forced convection due to a rotating crystal: the liquid is forced outward by centrifugal acceleration and is replaced by a central flow from the bottom of the crucible up to the center of the rotating crystal (*fig. 1.3b*)
3. Forced convection due to a rotating crucible: here the liquid flow is the same as for thermal convection except that the upward flow is spiral in form (*fig. 1.3c*)
4. Combined liquid rotation and thermal convection: in this case thermal convection is discouraged by a Coriolis stabilizing force acting on particles having a horizontal velocity component.

Monitoring of the flux convection is very important during the growth in order to minimize the presence of stress in the crystal.

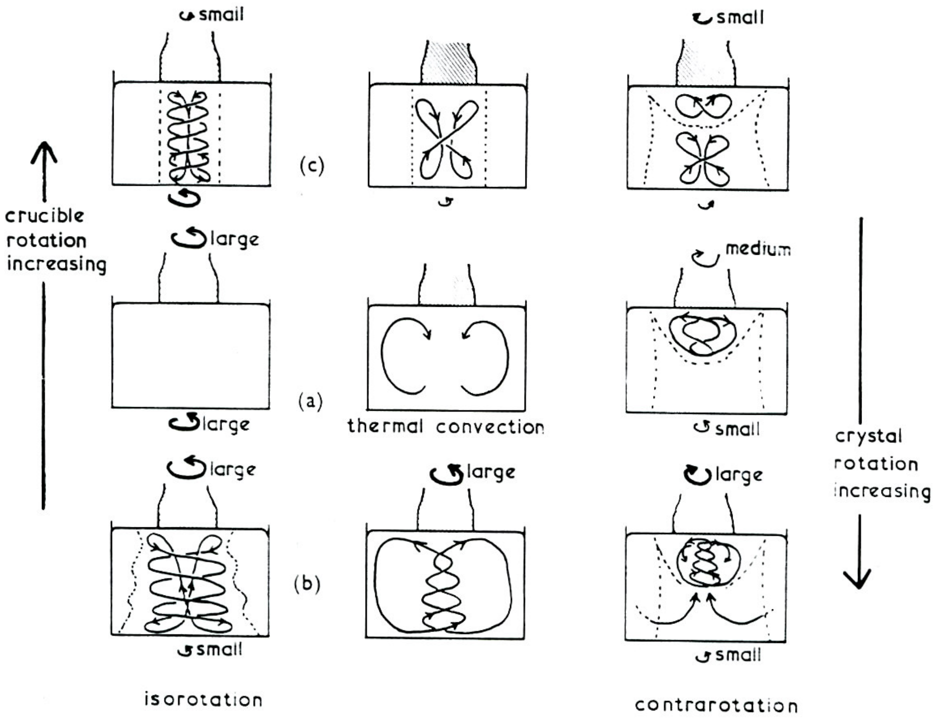

Fig.1.3: *Flow patterns for different crystal and crucible rotation rate*

The choice of pull rate is dependent on a number of factors:

1. Diameter of crystal required.
2. Melt temperature.
3. Importance of dislocation inclusions.

Actually, if a large crystal is required, it should be considered that in this case a larger strain will be present and the dislocation density will be not negligible. The dislocation density also increases with increasing growth rate [1].

1.2. Samples and their applications

1.2.1 Neodymium doped YAG: a brief presentation of the most widely used laser medium

Yttrium Aluminum Garnet doped with Nd^{3+} ions ($Y_{3-x}Nd_xAl_5O_{12}$) is the most widely used solid state laser medium, with a wide variety of applications. The good properties of this material derive from its chemical-physical characteristics: it is clear, hard, optically isotropic. It has good mechanical strength, good thermal properties, and the ability to sustain a precise optical polish. Some important physical properties of Nd:YAG are reported in Table II [8].

	Nd:$Y_3Al_5O_{12}$ physical properties	
Property	**without activator**	**with Nd^{3+} ions (~ 1 at.%)**
Lattice constants (Å)	12.000	~12.01
Cation symmetry	Y^{3+} -(D_2) Al^{3+} -(C_{3i}) Al^{3+}_{II} -(S_4)	
Melting point (°C)	1970	
Debye temperature (K)	700-750	
Thermal conductivity ($W \cdot m^{-1} \cdot K^{-1}$)	13	11-14
Specific heat ($cal \cdot g^{-1} \cdot K^{-1}$)	0.14-0.15	
Thermal expansion coef., α (10^{-6} K^{-1})	8.2 (100) 7.7 (110) 7.8 (111)	~6.96
Thermal diffusion ($cm^2 \cdot s^{-1}$)	0.046	0.050
Molecular weight	539.59	
Density ($g \cdot cm^{-3}$)	4.55	4.55
Mohs Hardness	8.25-8.5	
Sound velocity (10^5 cm s^{-1})	8.5630 $(001)_l$ 5.0293 $(001)_s$ 8.6016 $(110)_l$	

Table II: *Nd:YAG physical properties*

Principal emission wavelengths of Nd:YAG are at 946 nm, 1064 nm, 1319 nm. Figure 1.4 shows the Nd^{3+} energy levels and the principal optical transitions observed in YAG at 77 K, 300 K and 600 K [8]. Kaminskii calculates the energy values of Nd levels and their transitions between 869 nm and 2130 nm.

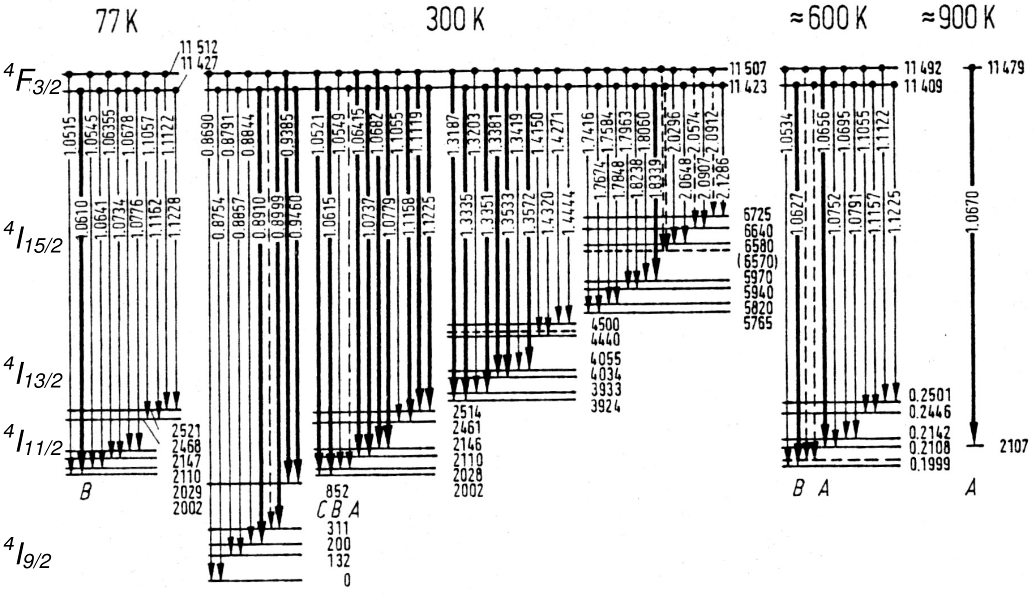

Fig. 1.4: *Nd:YAG energy levels*

Figure 1.4 reports the principal transitions that originate the laser emission at 1064 nm. These transitions starting from the sub-level R_2 of $^4F_{3/2}$ level end in the Y_3 Stark component of $^4I_{11/2}$ level.

At room temperature only 40% of the total $^4F_{3/2}$ level population is in the R_2 sub-level; laser emission occurs whenever R_2 is filled by thermal excitation at the expense of R_1 population [9].

Important optical properties of Nd:YAG are reported in Table III by Kaminskii.

Property	**$Nd:Y_3Al_5O_{12}$ optical properties** **without activator**	**with Nd^{3+} ions (~ 1 at.%)**
Elasto-optic constant	$p_{11} = -0.029$	
	$p_{12} = 0.0091$	
	$p_{44} = -0.061$	
Breaking strain (Kg cm-2)	1.75-2.1	
Optical transparency range (nm)	240-600	
Refractive index *n*	1.81523@1064nm	1.81633@1064nm
Linear dispersion dn/dT (10^{-6} K^{-1})	9.84±0.04	
Nonlinear refractive index n_2 (10^{-13} esu)	4.08	
Dielectric constants	$\varepsilon_0 = 11.7$	
	$\varepsilon_\infty = 3.5$	
Distribution coef. For Nd^{3+} ions	~0.18	

Table III: *Nd:YAG optical properties*

The analysis of experimental data shows that a low concentration of Nd^{3+} ions in YAG allows the formation of one type of activator center: Nd^{3+} replaces Y^{3+} cation (six magnetically non-equivalent site types in the unit cell) with D_2 symmetry. This condition ensures good performances in laser emission.

Figure 1.5 shows the absorption spectra of Nd:YAG in the 300-900 nm region [9].

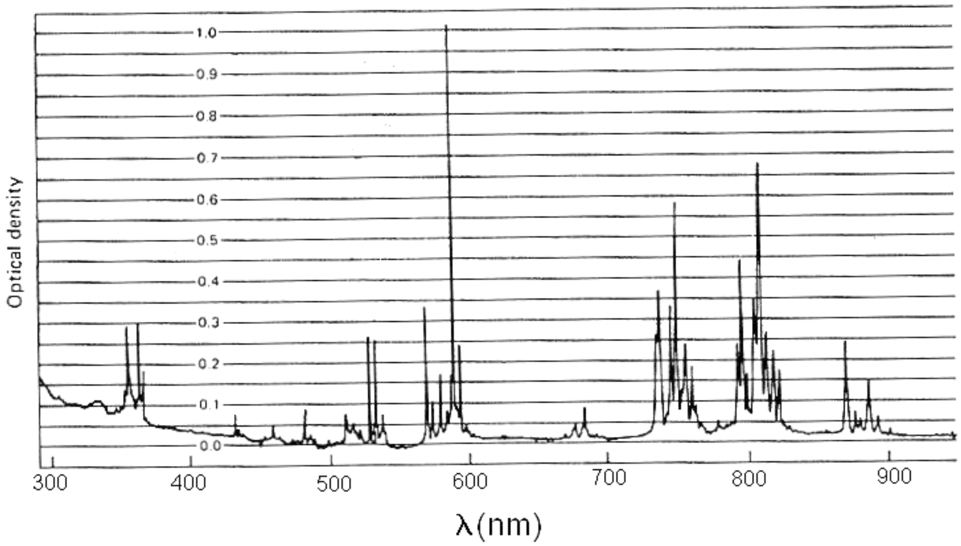

Fig. 1.5: *Nd:YAG absorption spectra*

Main pumping wavelengths for diode-pumped Nd:YAG crystals are centred at 808.6 nm and 885.0 nm. Figure 1.6 reports the absorption coefficient in the 790-825 nm range for three different Nd concentration in YAG: 1.0, 2.0 and 3.0 at % [10].

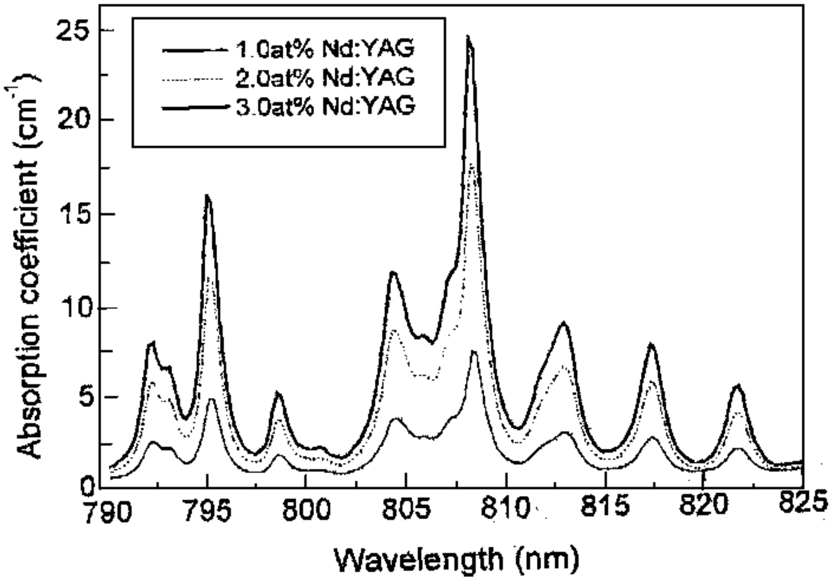

Fig. 1.6: *Absorption coefficient at different concentration*

Mao et al. [10], calculate the absorption coefficient at 808.7 nm for different concentrations: 7.3 cm^{-1} at 1 at.%, 17.5 cm^{-1} at 2 at.% and 24.3 cm^{-1} at 3 at. %.The optimum concentration of activator elements, for a given laser medium, has special importance because it determines the energetic parameters for laser operation. In order to find the optimum content of Nd^{3+} ions in YAG Kaminskii reported the luminescence intensity I$_{lum}$(C) at 300 K in a series of crystals with different concentrations. Analysing the behaviour of the $^4F_{3/2} \rightarrow {}^4I_{11/2}$ transition (1064 nm), he found that the maximum of luminescence intensity falls at C$_{opt}$ ≈ 1.1 at.%. The minimum threshold energy E$_{thr}$(C) to obtain laser emission at 1064 nm confirms the C$_{opt}$ value. Figure 1.7 shows these results.

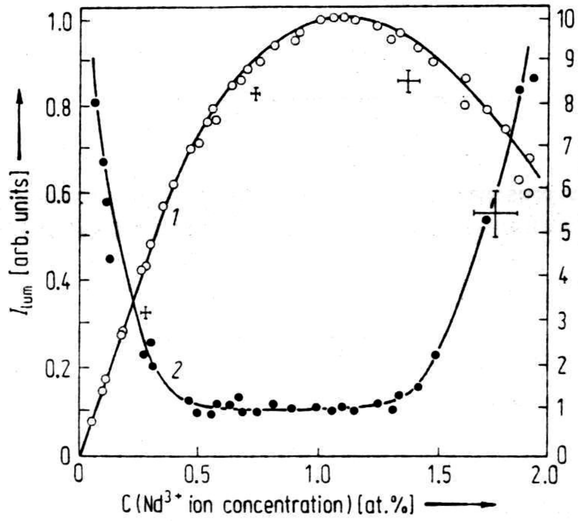

Fig. 1.7: *Luminescence intensity at1064 nm vs Nd concentration*

Absorption cross section for the 808.6 nm pumping wavelength is calculated by Pollnau in [11] and it corresponds to 3.3 10^{-20} cm^2, while the absorption and stimulated cross section of the fluorescence transition between 860 nm and 1450 nm are estimated by Singh et al. in [12]. Results are summarized in Tables IV and V, while the figure 1.8 shows the Stark components corresponding to the transition in Table IV.

λ (nm)	ν (cm^{-1})	Transition	$\Delta\nu$ (cm^{-1})	σ (10^{-20} cm^2)	β
869.0	11504	$R_2 \rightarrow Z_1$	13	4.2	0.033
875.4	11420	$R_1 \rightarrow Z_1$	10	1.1	0.013
879.2	113719	$R_2 \rightarrow Z_2$	18	1.3	0.017
884.4	11304	$R_2 \rightarrow Z_3$	19	4.2	0.036
885.8	11286	$R_1 \rightarrow Z_2$	19	3.5	0.066
891.1	11219	$R_1 \rightarrow Z_3$	10	2.4	0.040
893.4	11190	$R_2 \rightarrow Z_4$	31	0.5	0.004
900.0	11108	$R_1 \rightarrow Z_4$	31	1.2	0,037
938.6	10651	$R_2 \rightarrow Z_5$	10	4.8	0.030
946.1	10567	$R_1 \rightarrow Z_5$	9	5.1	0.040
1052.13	9502	$R_2 \rightarrow Y_1$	5	15.1	0.042
1055.05	9475	$R_2 \rightarrow Y_2$	5	1.1	0.006
1061.58	9422	$R_1 \rightarrow Y_1$	4	22.8	0.079
1064.18	9394	$R_2 \rightarrow Y_3$	5	45.8	0.135
1064.55	9391	$R_1 \rightarrow Y_2$	5	8.1	0.030
1068.26	9358	$R_2 \rightarrow Y_4$	10	6.7	0.036
1073.85	9310	$R_1 \rightarrow Y_3$	4	16.3	0.061
1078.0	9274	$R_1 \rightarrow Y_4$	9	4.6	0.045
1105.42	9044	$R_2 \rightarrow Y_5$	20	2.0	0.02
1112.12	8989	$R_2 \rightarrow Y_6$	14	3.6	0.025
1115.95	8959	$R_1 \rightarrow Y_5$	16	2.9	0.034
1122.7	8905	$R_1 \rightarrow Y_6$	13	3.0	0.030
1318.8	7581	$R_2 X_1$	6	8.7	0.018
1320.0	7574	$R_2 X_2$	6	1.9	0.004
1333.8	7495	$R_1 X_1$	6	3.0	0.009
1335.0	7489	$R_1 X_2$	6	3.4	0.009
1338.2	7471	$R_2 X_3$	6	9.2	0.021
1341.0	7455	$R_2 X_4$	9	3.5	0.011
1353.6	7386	$R_1 X_3$	7	1.4	0.005
1356.4	7370	$R_1 X_4$	8	4.4	0.0175
1414.0	7070	$R_2 X_6$	15	3.3	0.016
1430.8	6987	$R_1 X_6$	15	2.3	0.0145
1444.0	6923	$R_1 X_7$	10	3.4	0.0162

Table IV: *cross-section at different wavelength*

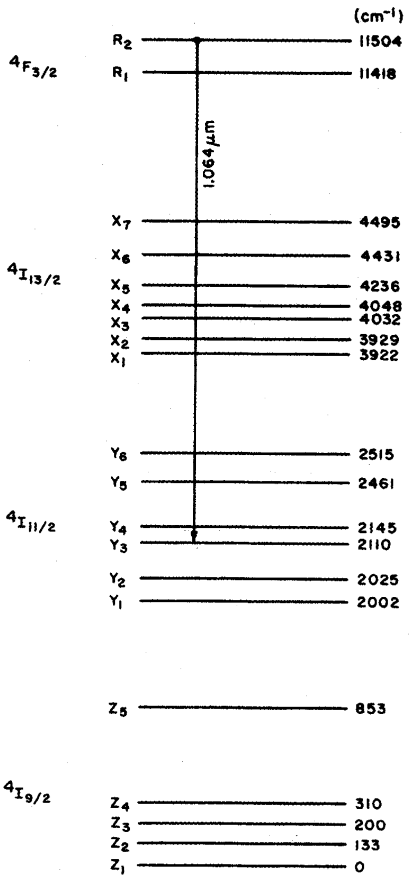

Figure 1.8: *Stark component of Nd^{3+} in YAG*

Wavelength (nm)	Transition	Nd^{3+} density in initial level (cm^{-3})	Peak α (cm^{-1})	Peak σ (10^{-20} cm^2)
869.0	$R_2 \rightarrow Z_1$	6.45×10^{19}	2.7	4.2
875.4	$R_1 \rightarrow Z_1$	6.45×10^{19}	0.7	1.1
879.2	$R_2 \rightarrow Z_2$	3.41×10^{19}	0.4	1.2
884.4	$R_2 \rightarrow Z_3$	2.47×10^{19}	1.27	5.1
885.8	$R_1 \rightarrow Z_2$	3.41×10^{19}	1.3	3.8
891.1	$R_1 \rightarrow Z_3$	2.47×10^{19}	0.58	2.3
900.0	$R_1 \rightarrow Z_4$	1.46×10^{19}	0.16	1.1
938.6	$R_2 \rightarrow Z_5$	1.08×10^{18}	0.05	4.5
946.1	$R_1 \rightarrow Z_5$	1.08×10^{18}	0.05	4.8

Table V: *emission cross section at different wavelength*

Mentioned absorption and stimulated cross sections are estimated at room temperature for a sample of 14×13.6×1.875 mm^3 with 3 at.% concentration of Nd^{3+} ions. These parameters are very important in order to analyze the behavior of each transition at different pumping conditions.

An additional significative parameter was reported by Kaminski [8] who analysed the dependence of the relative quantum yield of Nd^{3+} ions in YAG crystal as a function of excitation wavelength. Measurements concerned the $^4F_{3/2} \rightarrow {}^4I_{11/2}$ transition with an activator concentration of about 1 at.% (Fig 1.9). The figure shows that the quantum efficiency is almost constant at about 0.65 for all the excitation wavelengths.

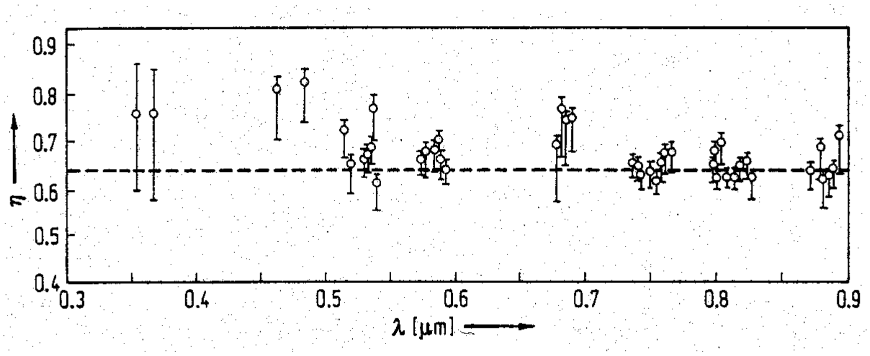

Fig. 1.9: *quantum yield vs excitation wavelength*

Luminescence lifetime value of the $^4F_{3/2}$ level has an important dependence on the temperature and the concentration of Nd^{3+} ions in YAG. Figure 1.10(a-d) shows the temperature dependence of luminescence lifetime of the $^4F_{3/2}$ level, for samples with different Nd concentration of 1.0, 1.5, 2.0 and 3.0 at.% [10]. While luminescence lifetime of the $^4F_{3/2}$ level in the 1.0 at% sample is almost temperature independent (fig.1.10-a), at higher concentrations (1.5, 2.0 and 3.0 at% Nd:YAG) it decreases as the temperature increases up to 100K.

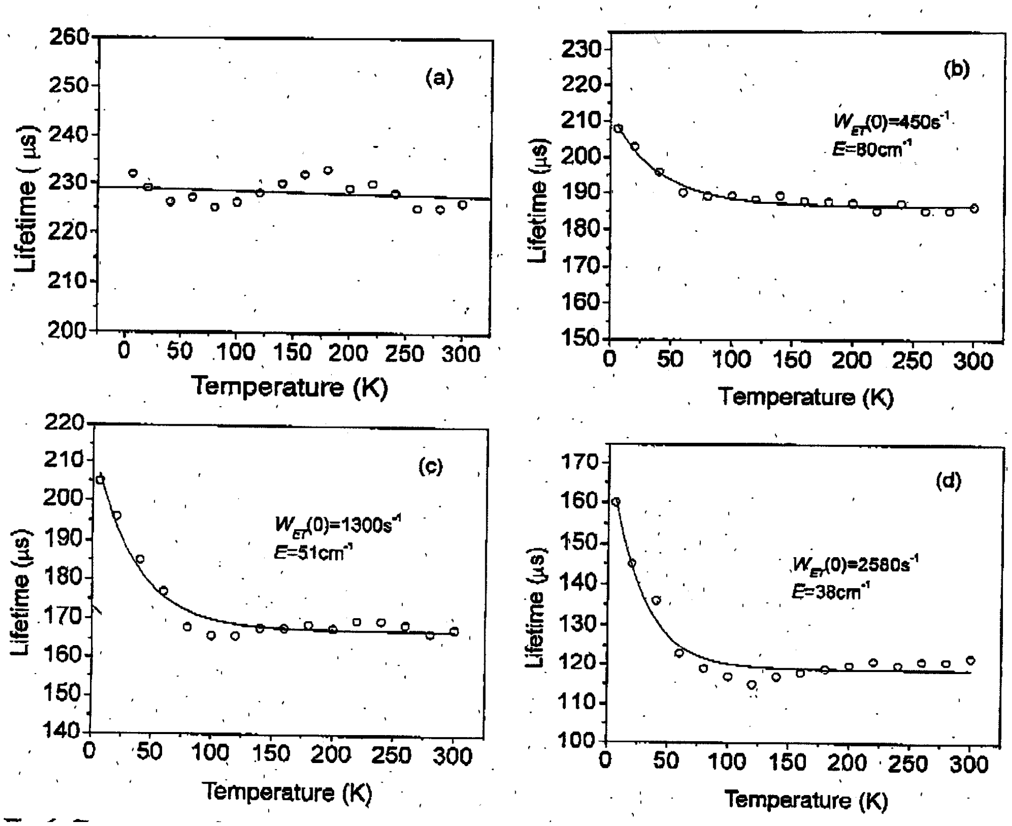

Fig.1.10: *Temperature dependence of the* $^4F_{3/2}$ *level fluorescence lifetime for different Nd ion concentration in YAG crystals, a)1.0, b)1.5, c)2.0, d) 3.0 at% Nd*

In addition the same authors estimated the relative quantum efficiency of these samples at room temperature by using the fluorescence lifetime [10]. This parameter decreases significantly with Nd concentration, and this reduction is ascribed to a concentration quenching associated with the cross-relaxation ion-ion interaction (fig. 1.11).

Kaminskii [8] reported the concentration dependence of the quantum efficiency in the 0.1 -10 at% concentrations range (fig.1.12).

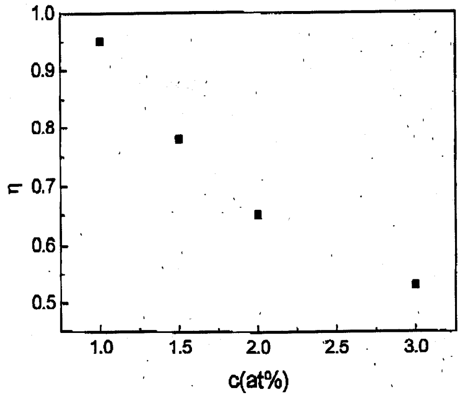

Fig.1.11: *Quantum efficiency vs dopant concentration*

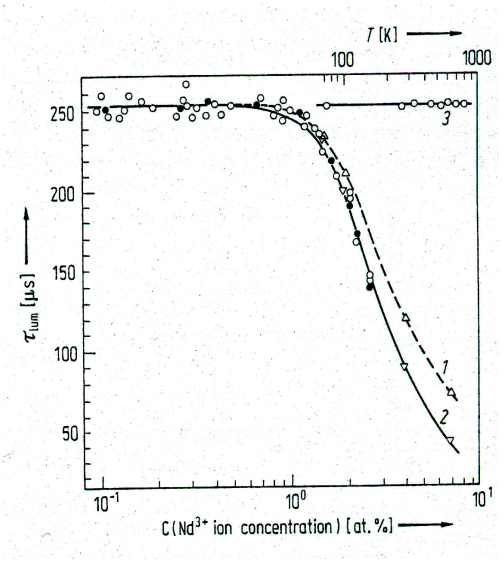

Fig. 1.12: *luminescence lifetime vs dopant concentration*

This study allows to verify the threshold limit of 1 at% Nd concentration in YAG single crystals. Above that threshold the efficiency of the active medium is largely decrease.

Table VI summarizes the results obtained for the Nd:YAG 1064 nm laser emission with 885 and 808 nm pumping [13]. The active medium was located in a 25 mm plane-concave resonator with an output mirror of 50 mm curvature radius and 90%, 95%, 97%, or 99% reflectivity at 1064 nm. Neodymium concentration

Results for 1064nm laser emission under 885 nm or 808 nm pumping

C_{Nd} (at.%)	Lifetime τ(μs)	Sample thickness (mm)	Pump Wavelength λ_p (nm)	Absorbed pump power fraction	Threshold (mW)		Slope efficiency		Total optical losses L
					In incident power	In absorbed power	In incident power	In absorbed power	
1	205.4	3.0	885	0.36	86.1	31	0.2	0.54	0.01
			808	0.91	78.0	71	0.45	0.49	
2.4	117	3.0	885	0.59	76.3	45	0.3	0.50	0.028
			808	0.99	74.5	73	0.46	0.46	
3.5	91	1.0	885	0.41	158.5	65	0.19	0.46	0.04
			808	0.92	79.3	73	0.39	0.42	

Table VI: *emission of 1064 nm under 885nm and 808 nm pumping*

(C_{Nd}) and sample thickness are reported in Table VI.

In order to make a comparison to a standard 1 at.% Nd YAG sample (3.0 mm thick), Figure 1.13 displays the laser emission power versus the absorbed power for uncoated 2.4 at.% (3.0 mm thick) and 3.5 at.% (1.0 mm thick) samples under 885 nm pumping [13]. A decrease of slope efficiency and an increase of the absorbed power threshold with increasing C_{Nd} is noticed. The 1 at.% sample slope efficiency of 0.54 and the absorbed power threshold of 31 mW have to be compared with the slope efficiency of 0.50 and 0.46 and the absorbed power threshold of 45 mW and 65 mW for the 2.4 at.% and 3.5 at.% samples respectively.

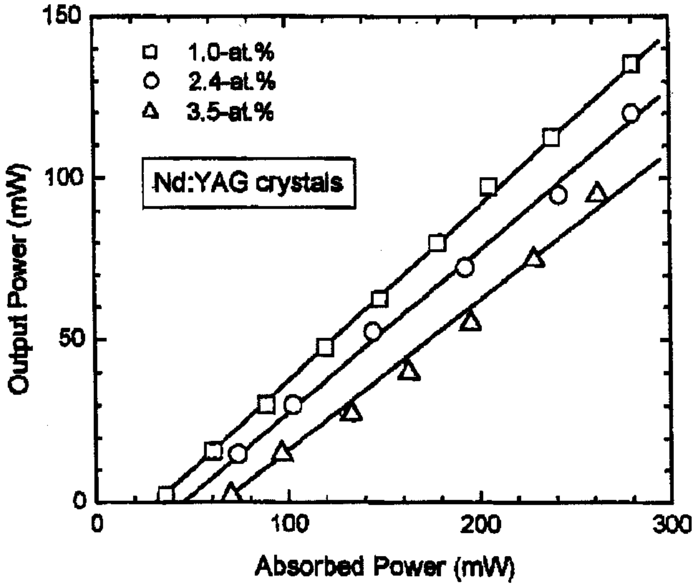

Fig. 1.13: *Output power vs pump power for different* Nd^{3+} *concentration*

1.2.2 Fe^{3+} doped YAG crystals

Among the different possible doping ions, the sensitising effect of trivalent ions, like Cr^{3+} or Fe^{3+} transition metals, is well known and was investigated in the last decades [14-20]: for example iron ions in Neodymium doped YAG crystal modify the ultraviolet (UV) optical absorption of the host material near the band edge; as a result the dependence of the efficiency on the spectral distribution of the pumping flash lamps is reduced due to the energy transfer between Fe^{3+} and Nd^{3+} ions [17,19-30].

At this purpose we have analyzed different samples of YAG, doped with Fe^{3+} ions, in order to understand the behavior of this transition metal respect to the host materials and its possible role as *sensitizer* element.

In order to understand the energy-level structure and the processes of energy transfer of optical centers formed by iron ion, we studied the Electron Phonon-Coupling (EPC) of Fe^{3+} ions in YAG crystals. Both the linear and quadratic contribution to the EPC were taken into account in order to have a complete understanding of the temperature dependence of the electrons phonons interaction.

The analysis of the linear and quadratic EPC constants of Fe^{3+} ions in YAG crystal was performed by studying the position, intensity and width of the zero phonon line transition of Fe^{3+} (800 nm) and its vibronic replicas as a function of the temperature in the range 9-150 K.

It will be shown in Chapter 5 that the study of the zero phonon line is a reliable and a relatively easy method to study the electron phonons coupling strength.

1.2.3 Mixed Garnet Laser for Water Vapour DIAL Transmitter

The development of new solid-state lasers, especially those operating between 0.9 and 3.0 µm, has renewed general interest in the optical properties of rare-earth ions (Re^{3+}) in garnet structure [9,31,32]. The energy levels of several Re^{3+} ions inserted as dopants in different garnet compounds, like Yttrium Aluminum Garnet (YAG) or Yttrium Scandium Gallium Garnet (YSGG), were successfully analyzed over the past years [33,34]. As illustrated in the previous paragraph 1.2.1, Neodymium-doped YAG is one of the most important available laser active medium for research and technological applications.

The prospective of enhancing efficiency and tunability of solid state lasers boosted the study of new materials able to meet specific technological purposes. Among the possible sources, mixed garnet host materials, like $Y_3Al_5O_{12}$ (YAG), $Y_3Sc_2Ga_3O_{12}$ (YSGG), $Gd_3Sc_2Ga_3O_{12}$ (GSGG) and $Y_3Sc_2Al_3O_{12}$ (YSAG), doped with lanthanides allow the so-called compositional tuning. By changing the material composition the lattice parameters can be modified leading to a variation of the strength of the crystal field. As a consequence, the emission wavelengths of a selected Re^{3+} ion can be tuned at request. Recently, Walsh et al. obtained over 100 mJ at 0.9441 µm in Q-switched mode from $Nd{:}YAG_{(0.18)}YSAG_{(0.82)}$ [35].

One of the main applications of mixed garnet materials is related to the remote sensing of the atmosphere. As an example, light detection and ranging (LIDAR) or differential absorption lidar (DIAL) techniques can be applied to determine molecular constituent concentrations present in the atmosphere, such as water vapor (H_2O) [36].

The possibility of tuning the laser emission to the right wavelength and investigating the desired molecule easily explains the growing interest in compositional tuning of mixed garnet materials [37,38]. This interest involves the design and the realization of devices able to emit laser light in the region of water vapour absorption lines (WALES). For WALES the regions of about 935 nm, 942 nm, and 944 nm have been identified as the most suitable wavelengths, however, these laser designs are highly sophisticated.

The main objective of the WALES is to provide essential information on the distribution of atmospheric water vapour and aerosols in the troposphere and lower stratosphere (from 0 to 16 km altitude) for numerical weather prediction, climatology and atmospheric modeling. Absolute quantitative measurements of water vapour will be obtained over a large dynamic range (from 0.01 to 15 g/kg), with a high level of vertical resolution and accuracy not achievable by other systems. The spatial and temporal variation of water vapour will be directly sampled with global coverage, not only above and below optically thin clouds but also above cloud tops and in cloud gaps between dense clouds. The independent set of global water vapour profiles can be used to validate other measuring techniques such as operational passive infrared and microwave. Secondary informations can also be derived such as cloud tops and base heights, optical thickness, planetary boundary layer height, and surface reflectance. As indicated in the ESA report, three wavelength regions, each one with a suitable subset of four wavelengths, have been identified. The main WALES system realized is the nadir-pointing DIAL instrument, that performs differential measurements of absorption at four closely separated wavelengths, three of which are 'online' measurements at molecular absorption lines of water, and one 'off-line' measurement, where absorptions are significantly reduced. In this way, the different subintervals of the dynamic absorption range are addressed by dedicated on-line wavelengths.

The different on-line wavelengths possess different penetration depths, thus allowing measurements over different altitude intervals. The strongly absorbing water vapour lines are used for higher altitudes (low water vapour concentration) and the weakly absorbing lines are used for lower altitudes (high water vapour concentration).

Mixed Garnet lasers have a great potential to fulfill the requirements and to become the preferred transmitter concept for WALES, as indicated by the European Space Agency [39] and can be pumped directly with diode laser and use a direct approach to generate the required laser pulse characteristics without frequency conversion. Therefore no additional non-linear crystals are needed and a higher electric to optical efficiency is expected as well as single frequency operation using spectral tuning elements like etalons. The main problem of these devices concerns the space radiation energy absorbed by the crystal lattice. It causes color centers that may reabsorb the pump and laser wavelength and consequently reduce the laser gain considerably.

This problem has been resolved with the introduction in the host materials of co-dopants atoms, like transition metal or rare earth. Co-dopants such as chromium, iron and cerium are able to suppress the color centers and are candidates for effective radiation hardening (see also 1.2.2 paragraph).

1.2.4 Mixed crystals with YAG-YSGG composition

Among the possible mixed crystals, with garnet symmetry, we have analyzed different samples composed by the $Y_3Al_5O_{12}$ (YAG) and $Y_3Sc_2Ga_3O_{12}$ (YSGG) oxides.

In the case of mixed host, composed from YAG and YSGG garnets, Ga occupies tetrahedral sites, Sc is in octahedral positions and Al can occupy both tetrahedral and octahedral sites.

These mixed garnets, doped with Nd^{3+}, generates a blue-shift in the photoluminescence (PL) emission of Nd^{3+} with respect to the observed emission of the Re^{3+} ion in YAG [8].

The aim of the study is to investigate the PL emission of the Nd^{3+} in samples with mixed structure YAG_xYSGG_{1-x} as a function of the concentration of

YSGG and the vibrational properties related to this mixed composition. The experimental results are proposed in the Chapter 4.

Mixed garnet samples, doped with 1% at. of Nd, were grown in collaboration with Scientific Materials Europe (Italy) by Czochralski method with different composition of YAG_xYSGG_{1-x} host materials.

References

[1] Brian R. Pamplin “*Crystal Growth”* Ed.Pergamon Press, 497-520 (1980)

[2] J. Czochralski, *Z. Phys. Chem.* 92, 219 (1918)

[3] D.T.J. Hurle, B. Cockayne *“Handbook of crystal growth”* Vol.2 Ed. Elsevier (1994)

[4] D.T.J. Hurle, *Sol. State Electronics* 3, 37 (1961)

[5] A.B. Chase, *“Preparation and properties of solid state materials”* Vol. 1 Ed. Dekker (1971)

[6] D.P. Devor, R.C. Pastor and L.G. DeShazer, *J. Chem. Phys.* 81, 4104 (1984)

[7] V. Lupei and A. Lupei, Physical Review B, Vol. 61(12), 8087 (2000)

[8] A.A. Kaminskii, *Laser Crystals-Their Physics and Properties,* Springer-Verlag, New York (1981)

[9] W. Koechner, *Solid-State Laser Engineering,* Springer-Verlag 1996

[10] Y. Mao, P. Deng and F.Gan, *Physica status solidi* Vol.193(2), 329-337 (2002)

[11] M. Pollnau, P.J. Hardman *et al.,* Physical Review B Vol. 58 (24), 16076 (1998)

[12] S. Singh, R. G. Smith et al., Physical Review B Vol. 10(6), 2566 (1974)

[13] V. Lupei, N. Pavel et al., IEEE Quantum Electronics Letters Vol. 38(3), 240 (2002)

[14] Die Dong, Kuang Xiao-Yu, Guo Jian-Jun, Wang Hui, and Zhou Kang-Wei Phys. Rev. B 72, 073101 (2005).

[15] S.R. Rotman, C.Warde, H.L. Tuller and J. Haggerty J. Appl. Phys 66 3207 (1989).

[16] Y.F. Chen, K.T. Wu, Y.D. Yao, C.H. Peng, K.L. You and W.S. Tse Microelectr. Engin. 81, 329 (2005).

[17] M.V. Korzhik, M.G. Livshits, B.I. Minkov, and V.B. Pavlenko Sov J. Quantum. Electron 22, 24 (1992).

[18] M.V. Korzhik, M.G. Livshits, M. L. Meilman, B.I. Minkov, and V.B. Pavlenko Opt. Spectrosc. 70, 471 (1991).

[19] Yu. A. Voitukevich, M. V. Korzhik, V.V. Kuzmin, M.G. Livshits, and M.L. Meilman Opt. Spectrosc. 63, 810 (1987).

[20] M.V. Korzhik, M.G. Livshits, Kh, S. Bagdasarov, A.M. Kevorkov, T.A. Melkonyan, and M.L. Meilman Sov J. Quantum. Electron 19, 344 (1989).

[21] J. P. Hurrell, P.S. Porto, I.F. ChNG, s.s. Mitra and R.P. Bauman Phys Rev B 173 851 (1968).

[22] M.L. Meil’man, M.V. Korzhik V.V. Kuzmin, M.G. Livshits, Kh, S. Bagdasarov, and A.M. Kevorkov, Sov. Phys. Dokl. 29(1), 61 (1984).

[23] G.B. Scott, D.E. Lacklison, and J.L. Page Phys. Rev. B 10, 971 (1974).

[24] R. Urban, A. Putilin, P. E. Wigen, S.-H. Liou, M. C. Cross, P. C. Hammel, and M. L. Roukes Phys. Rev. B 73, 212410 (2006).

[25] A. S. Tatarenko, G. Srinivasan, and M. I. Bichurin Appl. Phys. Lett. 88, 183507 (2006).

[26] Y. V. Khivintsev, Bijoy K. Kuanr, Ian Harward, R. E. Camley, and Z. Celinski J. Appl. Phys. 99, 08P512 (2006).

[27] G. A. Melkov, V. I. Vasyuchka, Yu. V. Kobljanskyj, and A. N. Slavin Phys. Rev. B 70, 224407 (2004).

[28] A.A. Semenov, S.F. Karmanenko, B.A. Kalinikos, G. Srinivasan, A.N. Slavin, and J.V. Mantese Electron. Lett. 42, 641 (2006).

[29] A.P. Vink, A. Meijerink, J. of Phys. and Chem. of solids 61, 1717 (2000).

[30] A. Ellens, H. Andres, A. Meijerink, and G. Blasse Phys, Rev. B 55, 173 (1997).

[31] G. S. Pomrenke, P. B. Klein and D. W. Langer “Rare Earth Doped Semiconductors” MRS Pittsburg 1993

[32] V. Lupei, G. Aka and D. Vivien, Optics Communications 204, 399 (2002)

[33] J.B. Gruber, M.E. Hills, T.H. Allik, C.K. Jayasankar, John R. Quagliano and F.S. Richardson, Phys. Rev. B 41, 7999 (1990)

[34] B.M. Walsh, N.P. Barnes, R.L. Hutchenson, R. W. Equall and B. Di Bartolo, J.opt. Soc. Am. B 15, 2794 (1998)

[35] B.M. Walsh, N.P. Barnes, R.L. Hutchenson and R. W. Equall, IEEE Journal of Quantum electronics 37, 1203 (2001)

[36] W.B. Grant, “Lidar for atmospheric and hydrospheric studies” in Tunable Laser Application, F.J. Duarte, Ed. New York: Marcel Dekker 1995, p.241

[37] N.P. Barnes, B.M. Walsh and R.L. Hutchenson, Advanced Solid State Laser 1, 522 (1996)

[38] F.S. Ermeneux, R. W. Equall, R.L. Hutchenson, R.L. Cone, R. Moncorge, N.P. Barnes, H.G. Gallagher and T. P. Han, Advanced Solid State Lasers 26, 242 (1999)

[39] R. Treichel, European Space Agency, ESA SP 554, 639-642 (2004)

CHAPTER 2

Vibrational properties of garnet structure

2.1 Elements of group theory

The geometric configuration of a physical system plays an important role in determining many of its properties. A configuration is determined by specifying the location of each part of the system relative to some coordinate frame. A symmetry operation is a coordinate transformation that leaves the system to locking exactly the same.

The set of all symmetry operations for a given system is said to be the symmetry of the system. The mathematical formalism that governs the properties of symmetry operations is the group theory [1,2].

Since the complete Hamiltonian operator of a system describes its physical properties, it must be the same before and after a symmetry operation and therefore is “invariant” with respect to the transformation. The Schrödinger equation is solved to obtain a set of eigenvalues and eigenfunctions for the system,

$$E_n = \langle \psi_n | H | \psi_n \rangle \qquad (2.1)$$

A symmetry operation O leaves H invariant, that is, the similarity transformation yields $H=O^{-1}HO$. The transformed eigenfunctions

$$|\varphi_n\rangle = O|\psi_n\rangle = |O\psi_n\rangle \qquad (2.2)$$

belong to the same eigenvalues E_n,

$$
\begin{aligned}
&E_n = \langle \psi_n | H | \psi_n \rangle = \langle \psi_n | O^{-1} H O | \psi_n \rangle = \langle \psi_n | O^{\dagger} H | \psi_n \rangle = \\
&\langle O\psi_n | H | O\psi_n \rangle = \langle \varphi_n | H | \varphi_n \rangle
\end{aligned}
\tag{2.3}
$$

If ψ is non degenerate, ψ and φ differ at most by a phase factor. This phase factor disappears when the eigenvalues is evaluated since

$$
\begin{aligned}
&\langle \varphi_n | \varphi_n \rangle = \langle O\psi_n | O\psi_n \rangle = \langle \psi_n | O^{\dagger} O | \psi_n \rangle = \langle O\psi_n | O^{-1} O | \psi_n \rangle = \\
&\langle \psi_n | I | \psi_n \rangle = \langle \psi_n | \psi_n \rangle
\end{aligned}
\tag{2.4}
$$

For a set of degenerate orthonormal eigenfunctions corresponding to eigenvalues E_n any normalized linear combination of $\psi_1, \ldots, \psi_n$ will also have the eigenvalue E_n, where

$$
E_n = \langle \Psi_I | H | \Psi_I \rangle,
$$

$$
|\Psi_I\rangle = \sum_{i=1}^{n} a_i |\psi_i\rangle, \quad \therefore \langle \Psi_I | \Psi_I \rangle = \sum_{i=1}^{n} |a_i|^2 \langle \psi_i | \psi_i \rangle = 1 \tag{2.5}
$$

with $|\Psi_I\rangle$ normalized and $a_1^2 + a_2^2 + \ldots + a_n^2 = 1$. There are n possible linear, orthogonal combinations. A symmetry operation applied to one of the wave functions takes it, in general, into a linear orthogonal combination of the degenerate functions,

$$
O\begin{pmatrix} |\psi_1\rangle \\ |\psi_2\rangle \\ \vdots \\ |\psi_n\rangle \end{pmatrix} = \begin{pmatrix} a_{11}|\psi_1\rangle + & a_{12}|\psi_2\rangle + & \cdots & + a_{ln}|\psi_n\rangle \\ a_{21}|\psi_1\rangle + & \cdots & & \\ \vdots & & & \\ a_{n1}|\psi_1\rangle + & \cdots & & + a_{nn}|\psi_n\rangle \end{pmatrix} \tag{2.6}
$$

Thus, for any physical system, if all symmetry operations leave a specific function unaltered except for a phase factor, that function transforms like a non-degenerate solution to the Schrödinger equation. If instead, some of the symmetry operations on a function create new, linearly independent functions, all these functions transform like members of a degenerate set of solutions to the Schrödinger equation.

The complete set of *h* symmetry operations for a system at a specific point in space forms the *point group* of the system, where *h* is called the order of the group. The symmetry operations of a group can be organized in *classes* where all elements of a class are related by an unitary transformation of some other group operator in the form [1,2]:

$$T^{-1}S'T = S'' \text{ where } T^{1}T = E.$$

Here S', S'', T^{-1}, T and E are all elements of the group and S'' and S' are in the same class. A *representation* is a set of matrices that multiply in the same way that the group elements multiply. The dimension of the representation is the order of the square matrices of the elements of the representation. The dimension of a representation is equal to its degeneracy. A similarity transformation can be used to put a matrix operator in a diagonal form,

$$\mathbf{A}' = \mathbf{T}^{-1}\mathbf{A}\mathbf{T} = \begin{pmatrix} \mathbf{A}_1 & & 0 \\ & \mathbf{A}_2 & \\ 0 & & \mathbf{A}_3 \end{pmatrix} \qquad (2.7)$$

where **A** and **A′** are matrices belonging to a *reducible representation* while the $\mathbf{A}_i$ are matrices belonging to an *irreducible representation*. There are always the same number of irreducible representations of a group as there are classes [1-3].

The *character* χ of an operator R in a specific representation is the trace of its matrix in that representation, $\chi(R)=Tr(R)=\sum_i R_{ii}$. The trace of a matrix is not changed by a similarity transformation, and thus all operators in the same class have the same characters. The character of a reducible representation is equal to the sum of the characters of the irreducible representations into which it can be decomposed. The number of times the *i*th irreducible representation appears in the decomposition of a reducible representation is given by

$$n^{(i)}=\frac{1}{h}\sum_{R}\chi_{R}^{(i)}\chi_{R}\,, \qquad (2.8)$$

where the sum is over all *R* symmetry operations of the group and h is the order of the group [1-3].

2.2 The O_h point group symmetry and Character Table

The most important point-group symmetry for solid state laser materials is O_h, which describes a regular octahedron with a center of inversion as shown in fig. 2.1 [2-6]. This is made up of 48 symmetry operation that can be grouped together in 10 classes [3,4]:

E: Identity
$3C_2$: 180° rotation on x, y, or z axis
$6C_4$: ±90° rotation on x, y, or z axis
$6C_4$: 180° rotation on axes parallel to the face diagonals
$8C_3$: ±120° rotation on body diagonals
i: Inversion

The inversion operation *i* is combined with each of the $C_2(=\sigma_h)$, $C_3(=S_6)$, $C_4(=S_4)$ and $C'_2\ (=\sigma_d)$ operations.

Therefore the O_h group has 4 three-dimensional irreducible representations, 2 two-dimensional irreducible representations, and 4 one-dimensional irreducible representations. The *character table* for the irreducible representation of the O_h group is presented in Table (VII).

O_h	E	$8C_3$	$6C2$	$6C4$	$3C_4^2=3C_2''$	$S_2=i$	$6S_4$	$8S_6$	$3\sigma_h$	$6\sigma_d$		
A_{1g}	+1	+1	+1	+1	+1	+1	+1	+1	+1	+1		$\alpha_{xx}+\alpha_{yy}+\alpha_{zz}$
A_{1u}	+1	+1	+1	+1	+1	-1	-1	-1	-1	-1		
A_{2g}	+1	+1	-1	-1	+1	+1	-1	+1	+1	-1		
A_{2u}	+1	+1	-1	-1	+1	-1	+1	-1	-1	+1		
E_g	+2	-1	0	0	+2	+2	0	-1	+2	0		$\alpha_{xx}+\alpha_{yy}-2\alpha_{zz}, \alpha_{xx}-\alpha_{yy}$
E_u	+2	-1	0	0	+2	-2	0	+1	-2	0		
T_{1g}	+3	0	-1	+1	-1	+3	+1	0	-1	-1	$(\mathbf{R}_x, \mathbf{R}_y, \mathbf{R}_z)$	
T_{1u}	+3	0	-1	+1	-1	-3	-1	0	+1	+1	$(\mathbf{T}_x, \mathbf{T}_y, \mathbf{T}_z)$	
T_{2g}	+3	0	+1	-1	-1	+3	-1	0	-1	+1		$\alpha_{xy}, \alpha_{yz}, \alpha_{xz}$
T_{2u}	+3	0	+1	-1	-1	-3	+1	0	+1	-1		

Table VII: *Character table of the O_h group*

The characters are determined by finding the traces of the transformation matrices for one element in each class using Eq. (2.7). For example, the character for the identity element will be the dimension of the irreducible representation, which is a direct consequence of the representation of E being an identity matrix of certain dimension. In this example, only the even-parity representation are shown. There is an equal number of odd-parity representation that have the same characters of each class of elements not involving the inversion operation –1 times the character of all classes of elements involving *i* [3]. These representations have the same designations as those shown except with an *u* (*ungerade*) subscript instead of *g* (*gerade*). Here *u* represent the anti-symmetric representations used to define basis functions possessing an odd parity with respect to an inversion operation.

One relevant procedure with the group character table is decomposing a product representation into irreducible representations. In the following paragraph the structure of garnet crystals, and their symmetry, are presented. The symmetry operation and the raman vibrational mode are analyzed by means of the illustrated O_h point group character table.

2.3 Host materials with garnet structure

The crystal structure of garnet belongs to the space group Ia3d (point group O_h^{10}), a body-centered cubic Bravais lattice member of the cubic O_h crystal class. The unit cell is composed by eight molecular units of $P_3Q_2(RO_4)_3$ [7]. Cations P,Q, and R have respectively 8, 6 and 4 nearest oxygen neighbors, and are situated at the 24*c* (blue), 16*a* (yellow) and 24*d* (green) Wyckoff positions in the unit cell (Figure 2.1).

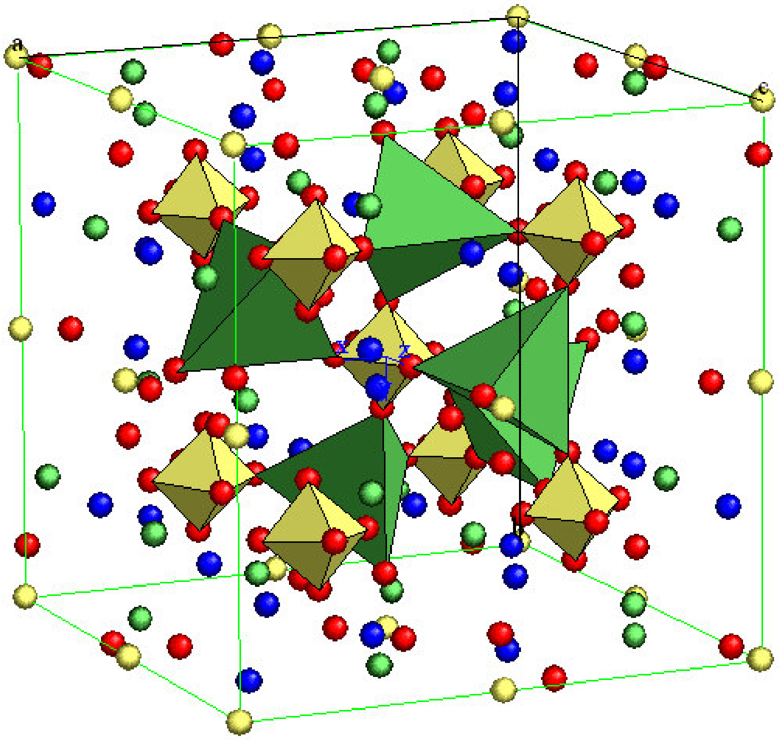

Fig.2.1: *Garnet structure*

The position of the 96*h* sites (red) of the oxygen anions depends upon three generic coordinates *x*, *y*, *z*. Interest in the garnet structures has been manly concentrated on composition where the same ions occupy the *a* and *d* sites and dopant elements are rare earth ions (Re^{3+}). Very attractive are the compositions where P cation can be one of the 14 rare earth ions or yttrium, and Q and R ions are Al, Ga, Fe or suitable atomic combinations [7-10].

The structure of the garnet compounds, with respect to the crystallographic axis, shows tetrahedral and octahedral coordination with central atoms in *d* and *a* sites respectively. These cations, for example the Al atoms in YAG, occupy eight octahedral sites of C_{3i} symmetry and twelve tetrahedral sites of S_4 symmetry. The Re^{3+} cations are placed in twelve dodecahedral sites of D_2 symmetry. The basic polyhedra of the garnet structure are presented in figure 2.2.

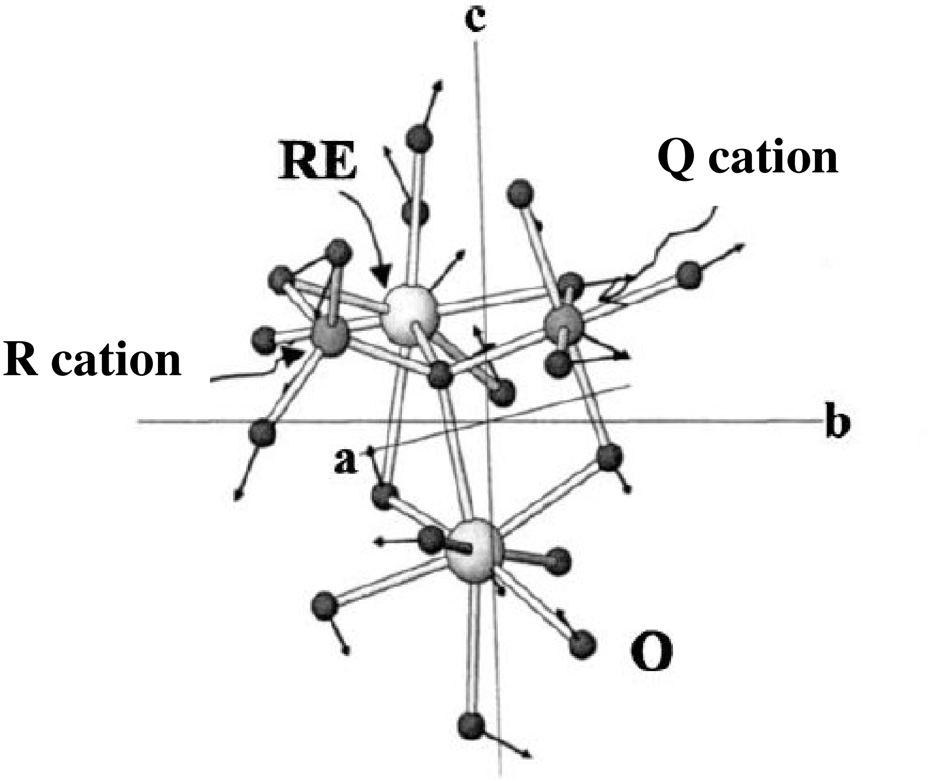

Fig.2.2: *Basic polyhedra of garnet structure*

As illustrated in the figure 2.2 each oxygen belongs to two dodecahedra, one tetrahedron, and one octahedron. The C*ation-O* distance in the tetrahedra is the shortest cation-anion distance, while in the octahedra is about 10% larger. The Re-O distances in the dodecahedra are 33% larger than the shortest *Cation*-O one. The oxygen polyhedra are not regular. The tetrahedra are distorted, being stretched along one of their fourfold rotary-inversion axes related to the tetrahedral symmetry, while the octahedra are stretched along the [111] axis of the unit cell [9].

By means of the character table and the above mentioned considerations on the structure of the garnet compounds, it is possible the determination of the irreducible representation relative to the O_h^{10} point group. The *usual* unit cell is quoted with twice the number of the occupied sites to illustrate the symmetry of the crystal rather than the full translational invariance including the equivalence of cube center and cube vertex sites. The representations derived from the character table are reduced to [4,7]:

$48(h \text{ sites}) \rightarrow 3(A_{1g}+A_{1u}+A_{2g}+A_{2u}+2E_g+2E_u+3T_{1g}+3T_{1u}+3T_{2g}+3T_{2u})$

$12(d \text{ sites}) \rightarrow A_{1u}+A_{2g}+E_g+E_u+2T_{1g}+2T_{1g}+3T_{1u}+3T_{2g}+2T_{2u}$

$12(c \text{ sites}) \rightarrow A_{2g}+A_{2u}+E_g+Eu+3T_{1g}+3T_{1u}+2T_{2g}+2T_{2u}$

$8(a \text{ sites}) \rightarrow A_{1u}+A_{2u}+2E_u+3T_{1u}+3T_{2u}$

Consequently the $k \approx 0$ modes are composed by the following symmetries:

$$\Gamma = 5A_{1u}+3A_{1g}+5A_{2u}+5A_{2g}+10E_u+8E_g+14T_{1g}+18T_{1u}+14T_{2g}+16T_{2u} \qquad (2.9)$$

In the cubic symmetry A_{1g}, E_g, T_{2g} modes are Raman-active and T_{1u} modes are IR-active. Therefore the irreducible representation is reduced in the form:

$$\Gamma = 3A_{1g}+8E_g+18T_{1u}+14T_{2g} \qquad (2.10)$$

that indicates the vibrational motion of all the structure that compose the garnet symmetry O_h^{10}. The figure 2.3 illustrates the principal vibrational modes relative to the Octahedra and Tetrahedra polyhedra in the structure [4,7].

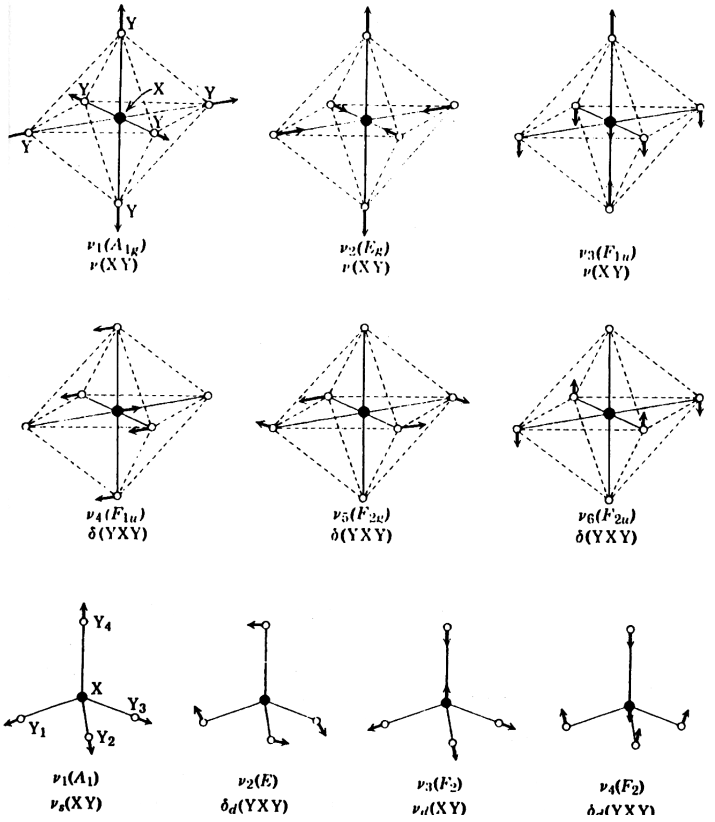

Fig.2.3: *Principal vibrational modes of the Octahedral and Tetrahedral structures*

The vibration frequencies depend principally on the atoms that constitute the unit cell. Different studies calculate the vibrational frequencies in many garnet structures by means of the rigid ion model and the free polyhedra approximation with the use of the Born-Mayer potential [8-10].

References

[1] M. Tinkham, *Group theory and Quantum Mechanics* Mcgraw-Hill, 1964
[2] R. C. Powell, *Physics of Solid State Laser Materials* AIP Press Springer, 1998
[3] H. Baranska et al, *Laser Raman Spectrometry,* Wiley 1987
[4] JR Ferraro and Kazuo Nakamoto, *Introductory Raman Spectroscopy*, Academic Press, San Diego, 1994
[5] A.A. Kaminskii, *Laser Crystals-Their Physics and Properties,* Springer-Verlag, New York (1981)
[6] W. Koechner, *Solid-State Laser Engineering,* Springer-Verlag 1996
[7] J.P. Hurrel, S.P.S. Porto, I.F.Chang, S.S. Mitra and R.P. Bauman, Phys. Rev. 173, 851 (1968)
[8] K. Papagelis, S. Vrs J. Appl. Phys 94 6491 (2003)
[9] K.Papagelis G. Kanellis S. Ves G.A Kourouklis Phys. Stat. sol. 233 134 (2002)
[10] K.Papagelis G. Kanellis, J. Arvanitidis, G.A Kourouklis S. Ves Phys. Stat. sol. 215 193 (1999)

CHAPTER 3

Crystalline field and Electron-phonon coupling

3.1 Crystal-Field Splitting of Energy levels

The first and primary objective of spectroscopic investigations on activated laser crystals is to analyze the Stark structure of the spectra and to establish the scheme of energy levels of the activator ions. The second stage of investigation is associated with determining the point symmetry group of the activator, symmetry properties of the wave function of the Stark levels, and selection rules for the optical transition and their intensities [1-3].

When a free ion is put into a crystal host, it is no longer in an environment of completely spherical symmetry. Instead it is surrounded by a set of nearest-neighbor ligands in some geometric configuration. In general the active dopant ion goes into the host substitutionally for a specific type of host cation and finds itself surrounded by oxide or fluoride anions. In a crystalline host the anions and cations are arranged on an ordered lattice with a well-defined symmetry. The host ligands and the dopant ions interact with each other through an electrostatic

Coulomb interaction. Using the fundamental concepts of group theory, recalled in Chapter 2, it is possible to predict the free-ion energy level splitting as a consequence of the crystal-field symmetry environment.

The dopant ion and the ligand can be considered to be point charges arranged in a geometric configuration. In these conditions the problem becomes one of calculating the Stark effect with a specific symmetry for the physical system.

According to [3] the Hamiltonian of an ion in a crystal field is given by:

$$H=\left(-\frac{\hbar^2}{2m}\sum_i \nabla_i^2-\sum_i \frac{Ze^2}{r_i}\right)+\sum_{j>i}\frac{e^2}{r_{ij}}+\sum_i \xi_i \mathrm{L}\cdot\mathrm{S}+$$
$$\sum_i eV_c\left(r_i,\theta_i,\varphi_i\right)=H_O+H_e+H_{SO}+H_c \qquad (3.1)$$

where the first term H_0, describing the interaction of each electron with the nucleus, is the unperturbed Hamiltonian. The other three terms are treated as successive perturbations and represent, respectively, H_e the Coulomb interaction of the electrons with each other, H_{SO} the spin-orbit interaction, and H_c the interaction of the electron with the crystal field of the ligands.

The various crystal fields that depend upon the relationship between H_e, H_{SO}, and H_c are generally divided into three types: weak fields ($H_c < H_{SO}$, H_e), medium fields ($H_e > H_c > H_{SO}$) and strong fields (H_{SO}, $H_e < H_c$). The weak crystal field case arises the Re and actinide ions whose inner unfilled 4*f* and 5*f* shells are compressed and shielded by outer filled $5s^2p^6$ and $6s^2p^6$ shells, respectively [2].

In the case of normal electron coupling ($H_e > H_{SO}$, RE ions), electrostatic electron interaction originates terms that are characterized by certain total orbital and spin angular moments (L and S). The spin-orbit interaction partially reduces the (2L+1)(2S+1) multiple-term degeneracy, and forms a multiplet structure of free-ion spectra [1]. In considering Stark splitting in a weak crystal field, the eigenfunctions $\left|L,S,J,J_z\right\rangle$ of the total momentum **J** = **L** + **S** are used as a basis of the zero-order approximation. This case is illustrated in Fig.3.1, which shows the scheme of energy level splitting (exemplified by the $^4I_{9/2}$ ground state) for the Nd^{3+} ion in a $Y_3Al_5O_{12}$ crystal.

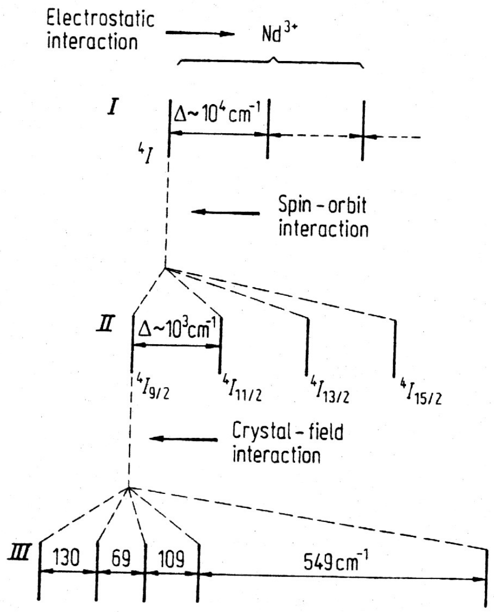

Fig. 3.1: *Level splitting scheme for Nd^{3+} ions in $Y_3Al_5O_{12}$ crystal.*

At medium crystal fields, it is possible to take the eigenfunctions $\left|L,L_x,S,S_x\right\rangle$ of the **L**, **S** operators as the zero-order wave functions.

In a medium crystal field, Stark splittings are smaller than the energy gaps between various terms of the same multiplicity (the same total spin) but larger than the fine-structure splitting in a free ion. Along with low-symmetry components of the crystal field, the spin-orbit interaction is generally treated as a perturbation that takes the cubic component of the crystal field into account [2,3].

A strong crystal field breaks the coupling between the orbital and spin momenta of electrons in the unfilled shell; an electron configuration in this case is determined by the occupation numbers of one-electron Stark levels whose energies are found by diagonalization of the V_c operator in the basis of one-electron functions $\left| l l_z \right\rangle$.

After the crystal-field splitting has been determined, multielectron crystal-field terms are constructed by taking into account the electrostatic interaction between the electrons.

The number of Stark levels in crystal fields of various symmetries depends on the quantum number *l* (strong field), *L* (medium field), and *J* (weak field), and is determined according to the group theory [1,4]. Table VIII lists the number of Stark components for various symmetries of the activator center for *J* running from 0 to 8 and from 1/2 to 17/2.

Local Symmetry	Point Group	J=0	1	2	3	4	5	6	7	8
		2J+1=1	3	5	7	9	11	13	15	17
Cubic	O_h, T_d, O, T_h, T	1	1	2	3	4	4	6	6	7
Hexagonal	D_{6h}, D_{3h}, C_{6v}, D_6, C_{6h}, C_{3h}, C_6	1	2	3	5	6	7	9	10	11
Trigonal	D_{3d}, C_{3v}, D_3, C_{3i}, C_3	1	2	3	5	6	7	9	10	11
Tetragonal	D_{4h}, D_{2d}, C_{4v}, D_4, C_{4h}, S_4, C_4	1	2	4	5	7	8	10	11	13
Orthorhombic	D_{2h}, C_{2v}, D_2	1	3	5	7	9	11	13	15	17
Monoclinic	C_{2h}, C_s, C_2	1	3	5	7	9	11	13	15	17
Triclinic	C_i, C_1	1	3	5	7	9	11	13	15	17
		J=1/2	3/2	5/2	7/2	9/2	11/2	13/2	15/2	17/2
		2J+1=2	4	6	8	10	12	14	16	18
Cubic	O_h, T_d, O, T_h, T	1	1	2	3	3	4	5	5	6
Other lower symmetry types		1	2	3	4	5	6	7	8	9

Table VIII: *Number of stark components for various symmetries*

In the calculation of the energy levels there are more difficulties with crystal-field operator of low symmetry. Therefore it is common to treat the first-order crystal-field perturbation as if the system had octahedral symmetry, and then treat lower symmetry cases as higher-order contribution to the crystal-field perturbation. These approximations have been very successful in treating solid-state laser materials.

Since the electronic wave functions have been expressed in terms of spherical harmonic functions, it is convenient to expand the operator V_c in terms of spherical harmonics [3],

$$V_c = \sum_j \sum_l \sum_m A_{lm} Y_l^m \left(\theta_j, \varphi_j\right) R_l \left(r_j\right), \tag{3.2}$$

where the subscript j designates the optically active electrons and the A_{lm} are expansion coefficients that depend on the specific lattice structure giving rise to the crystal field. The crystal-field operator must transform as the totally symmetric representation of the ion-ligand cluster in order that the total Hamiltonian remains invariant under all symmetry operation of the system.

To carry out crystal-field calculations in detail a specific symmetry must be assumed [3,4]. Consider, for example, the case of Nd^{3+} atoms in garnet structure, in which these cations occupy the center of a dodecahedron (c sites) with 8 oxygens as nearest-neighbors. In this case with D_2 symmetry, by assuming all the Ze-charged ligand ions as point charges, the electrostatic field at the c sites is given by:

$$V_c = \sum_i^8 \frac{Ze}{\left|\mathrm{r}_j - \mathrm{r}_i\right|} = \sum_i \sum_{l=0}^{\infty} \sum_{m=-l}^{l} \frac{4\pi Ze}{2l+1} \frac{r^l}{s^{l+1}} Y_l^{m^*} \left(\theta_i, \varphi_i\right) Y_l^m \left(\theta_j, \varphi_j\right) \tag{3.3}$$

where the standard multipole expansion has been used for $\left|\mathrm{r}_j - \mathrm{r}_i\right|^{-1}$. In the present case, **r**$_j$ is somewhere near the central ion and **r**$_i$ is the position of the ith ligand. The θ_i and φ_i are the polar coordinates of the ligands and the distance $|\mathbf{r}_i| = s > |\mathbf{r}_j|$. By comparing (3.2) and (3.3) one can obtain:

$$R_l(r) = \frac{r^l}{s^{l+1}} \quad \text{and} \quad A_{lm} = \frac{4\pi Ze}{2l+1}\sum_i Y_l^{m^*}(\theta_i,\varphi_i) \qquad (3.4)$$

The results of the calculation are expressed in terms of crystal-field parameters whose magnitude can be found by fitting the theoretical expression to experimental data. The radial function $R_l(r)$ and the angular coefficients can be determined with the use of geometrical configuration and tabulated spherical harmonic functions related to the cited symmetry.

3.2 Emission of Re^{3+} ions in Laser Crystals

Three possible mechanisms to explain the transition intensities of Re^{3+} ions in crystals are commonly used: electric quadrupole, magnetic dipole (*md*), and forced electric dipole (*ed*) emission [1,3].

The probabilities of forced electric dipole and magnetic dipole transitions may greatly exceed that of electric quadrupole transitions. Spectral-emission characteristics of laser crystals doped with Re^{3+} ions are mostly ascribed to forced electric dipole transitions [1]. The electric dipole transitions between levels of the same electronic configuration may be attributed to noncentrally symmetric interaction of the activator ion with the crystalline surroundings.

The probabilities for spontaneous electric dipole and magnetic dipole transitions are:

$$A^{ed}(i,j)=\frac{64\pi^4 v_{ij}^3}{3hc^3 g_i}\sum_{ij}\left|\langle i|P|j\rangle\right|^2,$$

$$A^{md}(i,j)=\frac{64\pi^4 v_{ij}^3}{3hc^3 g_i}\sum_{ij}\left|\langle i|M|j\rangle\right|^2, \qquad (3.5)$$

where $\langle i|\ |j\rangle$ are the matrix elements of the operators of the electric and magnetic dipole moments for the $i \to j$ transition. Thus, the only values in these expressions that depend on crystal properties are the dipole moments P and M [3].

The sum of the squared matrix elements in the above equations for spontaneous transition probabilities is called in spectroscopy the line (or transition) strength and is denoted:

$$S_{ij}=\sum_{ij}\left|\langle i|\ |j\rangle\right|^2 \qquad (3.6)$$

The probability for transitions between the ith and jth levels, or the Einstein coefficients in terms of transition strength, take the form [1]:

$$A_{ij}=\frac{64\pi^4 v_{ij}^3}{3hc^3 g_i}S_{ij},$$

$$B_{ji}=\frac{8\pi^3}{3h^2 g_j}S_{ij}, \qquad (3.6)$$

$$B_{ij}=\frac{8\pi^3}{3h^2 g_i}S_{ij}.$$

As illustrated the main problem concerning the transition intensity is the determination of the transition strength. By considering the transition between the states of the $4f^N$ electron configuration of an Re^{3+} ion inserted in a crystal field, the $\langle A|$ and $|A'\rangle$ states can be represented as linear combinations of the wave functions of the ground $4f^N$ configuration $\left|4f^N\psi JJ_z\right\rangle$ with the wave functions of excited $\left|\beta\right\rangle$ configurations of opposite parity [3]

$$\begin{aligned}\left\langle A\right| &= \left\langle 4f^N\psi JJ_z\right| - \sum_\beta \frac{\left\langle 4f^N\psi JJ_z\right|V_{cr}^{odd}\left|\beta\right\rangle\left\langle\beta\right|}{E\left(4f^N\psi JJ_z\right)-E(\beta)},\\ \left|A'\right\rangle &= \left|4f^N\psi' J'J'_z\right\rangle - \sum_\beta \frac{\left|\beta\right\rangle\left\langle\beta\right|V_{cr}^{odd}\left|4f^N\psi' J'J'_z\right\rangle}{E\left(4f^N\psi' J'J'\right)-E(\beta)}\end{aligned} \tag{3.7}$$

The operator of the electric dipole moment P can be expanded in the x, y, and z components of ($P_q^{(1)}$) which induce transitions of various polarizations. Non-zero matrix elements of the ($P_q^{(1)}$) operator relate the states of opposite parity admixed to $\left\langle A\right|$ and $\left|A'\right\rangle$

$$\begin{aligned}\left\langle A\right|P_q^{(1)}\left|A'\right\rangle = &-\sum_\beta \frac{\left\langle\psi JJ_z\right|V_{cr}^{odd}\left|\beta\right\rangle\left\langle\beta\right|P_q^{(1)}\left|\psi' J'J'_z\right\rangle}{E\left(4f^N\psi JJ_z\right)-E(\beta)} - \\ &-\sum_\beta \frac{\left\langle\psi JJ_z\right|P_q^{(1)}\left|\beta\right\rangle\left\langle\beta\right|V_{cr}^{odd}\left|\psi' J'J'_z\right\rangle}{E\left(4f^N\psi' J'J'_z\right)-E(\beta)}\end{aligned} \tag{3.8}$$

Here the summation is over all configuration-state components $\left|\beta\right\rangle$ of opposite parity.

The next significant step in developing the theory of Re^{3+} transition intensities concerns the use of the Judd-Ofelt approximation [3,5,6]. In this approximation the terms $E\left(4f^N\psi JJ_z\right)-E(\beta)$ and $E\left(4f^N\psi' J'J'_z\right)-E(\beta)$ are replaced with the constant *ΔE* independent of ψ, *J*, and β. This is equivalent to the assumption that electron configuration splitting is negligible compared with the energy gap between the levels.

Then the energy denominator is taken in (3.8) outside the summation sign, and the expression becomes:

$$\left\langle A\middle|P_q^{(1)}\middle|A'\right\rangle=\sum_{t,m}Y(t,m,q)\cdot\left\langle 4f^N\psi JJ_z\middle|U_{m+q}^t\middle|4f^N\psi'J'J_z'\right\rangle \qquad (3.9)$$

Here t is an even number; $\left\langle 4f^N\psi JJ_z\middle|U_{m+q}^t\middle|4f^N\psi'J'J_z'\right\rangle$ represents the matrix element of the $(m+q)$th component of the irreducible tensor operator of rank t; $Y(t, m, q)$ is the constant determined by

$$Y(t,m,q)=\sum_k(-1)^{m+q}(2t+1)^{1/2}A_{km}\begin{pmatrix}1 & t & k\\ q & -(m+q) & m\end{pmatrix}Z(k,t) \qquad (3.10)$$

where $Z(k, t)$ is the value proportional to the overlap integral of the radial parts of the wave functions for states belonging to the ground and excited electron configurations of the opposite parity and inversely proportional to the energy gap therein; A_{km} is the odd parameter of the crystal field potential ($k \le 7$) [1,3,5,6].

Summation of expression (3.9) over all J_z values of the initial and terminal states will remove the anisotropy associated with the polarization and yield the matrix element determining the probabilities for intermultiplet transitions. In this case, the expression for the line strength is

$$S^{ed}(\psi J;\psi'J')=\frac{1}{e^2}\sum_{J_zJ_z}\left|\left\langle A\middle|P_q^{(1)}\middle|A'\right\rangle\right|^2=\sum_{t=2,4,6}\Omega_t\left|\left\langle\psi J\middle\|U^{(t)}\middle\|\psi'J'\right\rangle\right|^2 \qquad (3.11)$$

Here the term $\langle \psi J \| U^{(t)} \| \psi' J' \rangle$ is a reduced matrix element of the irreducible tensor operator of rank *t* and Ω_t are the Judd intensity parameters determined by the expression:

$$\Omega_t = (2t+1)\sum_{k,m} |A_{km}|^2 Z^2(k,t)/(2k+1), \qquad (3.12)$$

where A_{km} are the odd parameters of the expansion of the crystal-field operator.

Thus, to describe the intensities of transitions observed in absorption and luminescence of crystals doped with Re^{3+} ions in this approximation, it is sufficient to have three parameters Ω_t (t = 2, 4, and 6). As a rule, these parameters are chosen from measured intermultiplet (integrated) absorption coefficients [1].

3.3 Electron –Phonon Interactions

The Electron Phonon Coupling (EPC) is the interaction between the electronic transitions of the emitting centers and the phonons of the host crystal [8-12]. At $T = 0K$ and $\vec{k} = 0$, no phonons are involved in the transition, that is the Zero Phonon Line (ZPL) transition is purely electronic, and the $n = 0$ vibrational state is the only occupied state. The intensity of the ZPL can be expressed as a Dirac delta function [10-12]:

$$I_{k=0}(T_{0K}, E) \propto \delta(\Delta E - E) \qquad (3.13)$$

where T_{0K} is the temperature at 0 K and ΔE is the energy difference between the fundamental level and the excited level.

In addition to the ZPL transition, there is also a finite probability that, in the final state, not only the vibronic modes of the impurity atom or molecule, but also those of the host system become excited. Transitions that correspond to a change in phonon state of the lattice ($\vec{k} \neq 0$) are called multi-phonon transitions. Multi-phonon transitions, in which n phonons participate, will lead to the appearance of a broad phonon sideband accompanying the ZPL.

In order to understand the thermal dependence of the transition due to the interaction with phonons, it is necessary to consider both the contributions related to the linear and quadratic coupling between electron and phonons.

In the linear coupling approximation, and in the limit of low temperatures, the basic features of the ZPL and the phonon sideband can be interpreted by the value of the Huang-Rhys parameter S

$$\frac{A_{ZPL}}{A_{ZPL} + A_{MP}} \cong e^{-S} \qquad (3.14)$$

where A_{ZPL} and A_{MP} are the integrated area of the ZPL and the multi-phonon transitions respectively. The Huang-Rhys factor gives the size of the vibrational relaxation energy and the strength of the electron-phonon coupling [10-12].

When the temperature increases the Debye approximation at finite temperature can be applied:

$$\frac{A_{ZPL}}{A_{ZPL} + A_{MP}} = \exp\left\{-S\left[1 + 4\left(\frac{T}{T_D}\right)^2 \int_0^{\frac{T_D}{T}} \frac{x}{e^x - 1} dx\right]\right\} \cong \exp\left\{-S\left[1 + \left(\frac{2\pi^2}{3}\right)\left(\frac{T}{T_D}\right)^2\right]\right\}$$

(3.15)

where T_D is defined as the Debye temperature and the approximation is valid in the limit of $T << T_D$.

In the low-temperature limit equation (3.15) reduces to equation (3.14). It follows from the above expressions that, when the temperature is increased, the integrated intensity of the ZPL has to decrease. By measuring the integrated intensity of the emission spectrum as a function of the temperature one can determine the Huang-Rhys parameter S and the Debye temperature T_D. However, in the linear approximation of EPC, the position and the line shape of the ZPL do not depend on the temperature and the interaction between electrons and optical phonons does not produce a shift of the ZPL [11-13]. Therefore, it is necessary to consider also the electron-phonon quadratic interaction terms between electrons and acoustic phonons to explain the broadening and the shift of the ZPL as the temperature increases.

The spectroscopic properties (line position and line shape) of ZPL depend on the temperature (T) and are determined by several contributions [7,9,11,14]. The peak position *E(T)* can be expressed as:

$$E\left(T\right)=E\left(T_{0K}\right)+\Delta E^{D}+\Delta E^{R}+\Delta E^{Orb} \qquad (3.16)$$

where the contributions to the line position due to one-phonon or direct process (ΔE^{D}), two-phonon Raman process (ΔE^{R}) and two-phonon resonant Raman process or Orbach process (ΔE^{Orb}) were considered. These contributions and their relative weight to the temperature dependence of the ZPL peak position are discussed in the following.

The term $E(T_{0K})$ is the position of the ZPL at $T=0K$.

The contribution ΔE^{D} is related to the direct transition with the absorption or the emission of one phonon. It can be expressed as:

$$\Delta E^{D}=\gamma_1\left(\frac{T}{T_D}\right)^2 P\int_0^{\frac{T_D}{T}}\frac{x^3}{\left(e^x-1\right)\left\{x^2-\left[\left(E_j-E_1\right)/k_bT\right]^2\right\}}dx \qquad (3.17)$$

where γ_1 expresses the linear coupling parameter for the transition between the E_1 and E_j states, k_b is the Boltzman's constant, T_D is the Debye temperature and P indicates the principal value of the integral. The expression above is evaluated in the Debye approximation of the phonon density by assuming that the phonon density $\rho(\omega)$ scales with ω^2, the square of the phonon frequency [12]. The numerical value of the Debye temperature T_D can be determined from the phonon cut-off energy, $\hbar\omega_{cutoff}$ (see Chapter 5). The contribution of the direct process to the line shift depends on the spectral separation of the two energy levels and the phonon cut-off energy of the crystal. A blue shift is reported when $\left(E_j - E_1\right)$ is comparable or larger than $\hbar\omega_{cutoff}$ and a red shift is observed in the other cases. As a general rule, the contribution to the thermal dependence of ΔE^D can be neglected with respect to the Raman one because the energy difference between *i* and *j* states is too large to be covered with a direct process [7,9,11,14].

In the Raman two phonons process, ΔE^R, the system (at the stationary level *i*) absorbs a phonon that bring the system to level *j'* then the system relaxes to the stationary level *j*. The energy differences $\Delta E_{ij'}$ and $\Delta E_{j'j}$ are much larger than the phonon energies in the crystal. By using the Debye approximation of phonon energies, it can be derived that the temperature-dependent contribution to the line position due to the Raman process is described by:

$$\Delta E^R = \alpha_E \left(\frac{T}{T_D}\right)^4 \int_0^{\frac{T_D}{T}} \frac{x^3}{e^x - 1} dx \tag{3.18}$$

where

$$\alpha_E = \frac{k_b T_D}{\hbar} \frac{3}{4\pi} \frac{w}{w+1} \tag{3.19}$$

is the electron-phonon coupling parameter for the Raman process and w is the quadratic coupling constant (w>-1) [7,9-11,14].

The contribution of the Orbach process (ΔE^{Orb}) arises from a resonant Raman two-phonon process, when the energy differences between levels *i*, *j*, and *j'* are in the range of the phonon energy of the crystal.

In a similar way to the line shift, different mechanisms should be considered to explain the line broadening with temperature, but the minor contribution of different terms can be neglected. The line width of the zero-phonon line is determined by the lifetime of the starting and final level. Linear electron-phonon interactions alone do not produce line broadening, neither does the coupling to the optical phonons, nor the thermal expansion [15]. In addition the phonon-phonon interactions are, in general, weaker than the electron-phonon coupling for optical transitions.

The expression of the dependence of the line width from the temperature contains only the contributions from the inhomogeneous line width (Γ^{inh}), the one-phonon direct process (Γ^{D}), the Raman two-phonon process (Γ^{R}) and the radiative transition (Γ^{rad}) [7,9,11,14,16]:

$$\Gamma(T) = \Gamma^{inh} + \Gamma^{D}(T) + \Gamma^{R}(R) + \Gamma^{rad}(T) \tag{3.20}$$

The inhomogeneous broadening Γ^{inh} is mainly due to strain and defects in host lattice and in first approximation is possible to consider it as temperature independent. Because of the random probabilities of the recombination due to the inhomogeneous processes the curve shape is a Gaussian.

Γ^{D} is the contribution due to the direct or one-phonon process: one phonon is emitted or absorbed. This contribution is described by

$$\Gamma^{D}(T) = \Gamma^{D}_{em}(T) + \Gamma^{D}_{as}(T) = \sum_{j<i} \beta_{ij}(n+1) + \sum_{j>i} \beta_{ij}(n) \tag{3.21}$$

In this equation, β_{ij} is a coefficient of the EPC for the direct process, $n = \left[\exp\left(\Delta E_{ij} / k_b T\right) - 1\right]^{-1}$ is the phonon occupation number, *i* and *j* are two vibrational energy levels. The energy gap between the states *i* and *j* is in the range of the phonon energies of the system. Direct process causes Lorentzian broadening of the line shape because of the energy dependent one phonon relaxation rate.

By using the Debye approximation of the phonon energies, the contribution of Raman two-phonon relaxation can be expressed by

$$\Gamma^R(T) = \alpha_\Gamma \left(\frac{T}{T_D}\right)^7 \int_0^{\frac{T_D}{T}} \frac{x^6 e^x}{\left(e^x - 1\right)^2} dx \qquad (3.22)$$

where

$$\alpha_\Gamma = \frac{k_b T_D}{\hbar} \frac{9}{4} \left(\frac{w}{w+1}\right)^2 \qquad (3.23)$$

is the EPC parameter for the Raman process [7,9,11,14,16].

The last term, Γ^{rad} is the contribution due to the radiative relaxation of a state.

3.4 Sensitized-Crystal laser

Several methods have been suggested for improving the efficiency of crystal laser. Among them the sensitizing method is of particular interest. Along with the main activator ions, ions of another type are also introduced into a crystal, the so-called *sensitizers* or *donors* (D). Their function is to absorb the excitation energy and transfer it to the main ions, *acceptors* (A). This process can be represented in the scheme:

$$\mathbf{D_{exc} + A \rightarrow D + A_{exc}} \qquad (3.24)$$

where the subscript "*exc*" represents an excited state of a given ion [3,17].

Thanks to the additional absorption bands of the sensitizing ions, the effective pumping band will be extended in the case of broad-band optical excitation. Hence, the excitation threshold decreases, while the emitting-ion intensity increases (sometimes rather largely).

The most effective energy transfer from donors to acceptors occurs when the donor emission spectrum is in resonance with the acceptor absorption spectrum. How much their spectra overlap is shown by a parameter known as the overlap integral,

$$\int \frac{A_D(E)\sigma_A(E)}{E^4} dE . \qquad (3.25)$$

Here the term $\int A_D(E)dE = 1/\tau_{rad}^D$ is the spontaneous-emission probability of the donor ions, where E is the photon energy, $\tau^D{}_{rad}$ is the radiative lifetime measured at low concentration of the sensitizing ions, and $\int \sigma_A(E)dE = Q_A$ is the integrated cross section, proportional to the area covered by the absorption curve, which is due to transition between the acceptor-ion states involved in excitation-energy transfer [17,18].

The probability of the excitation-energy-transfer is due to different factors. In the case of electric dipole transitions, which are most typical for the activator and sensitizing ions (Re^{3+}) used in laser crystals, this probability takes the form [1]:

$$P_{ed} = \frac{3\hbar^3 c^4}{4\pi n^4} \frac{1}{R^6} \frac{Q_A}{\tau_{rad}^D} \int \frac{F_A(E) f_D(E)}{E^4} dE . \tag{3.26}$$

In this case, with equal statistical weights of the levels involved in the process and broad spectral bands, the term R represents the donor-ion/acceptor-ion distance; the form $\int F_A(E)dE = 1$, because it is assumed that $\sigma_A(E) = Q_A F_A(E)$; and $\int f_D(E)dE = 1$ under the condition $1/\tau_{rad}^D = A_D f_D(E)$.

More often, however, the transition involved in the energy transfer are not in resonance; nevertheless, experiments show this process to be rather effective. Investigations have revealed that, in this case, the energy transfer process also involves phonons of the crystal. In this condition the parameters of electron-phonon coupling (see the paragraph 3.3) play an important role in the phono-assisted sensitizing process.

References

[1] A.A. Kaminskii, *Laser Crystals-Their Physics and Properties,* Springer-Verlag, New York (1981)

[2] W. Koechner, *Solid-State Laser Engineering,* Springer-Verlag 1996

[3] R. C. Powell, *Physics of Solid State Laser Materials* AIP Press Springer, 1998

[4] M. Tinkham, *Group theory and Quantum Mechanics* Mcgraw-Hill, 1964

[5] B.R. Judd, Phys. Rev 127, 750-762 (1962)

[6] G.S. Ofelt, J. Chem. Phys 37, 511-520 (1962)

[7] A. Ellens, H. Andres, A. Meijerink, and G. Blasse Phys, Rev. B 55, 173 (1997).

[8] Baldassarre Di Bartolo, *Optical Interactions in Solids* (Wiley, New York,1968), chap. 15.

[9] Richard C. Powell, *Physics of Solid-State Laser Materials* (Springer-Verlag, New York, inc. 1998), chap. 4-5.

[10] H. Wang, F.D. Medina, D.D. Liu, and Y.D. Zhous, J. Phys.: Condens. Matter 6, 5373 (1994).

[11] J.L. Skinner, and D. Hsu Adv. Chem. Phys. 65, 1 (1986).

[12] G.P. Srivastava *The Physics of Phonons* (Adam Hilger, IOP, New York, 1990), chap. 2-7.

[13] D. Hsu, and J.L. Skinner J. Chem. Phys. 81, 1604 (1984).

[14] M.G. Beghi, C.E. Bottani, and V. Russo J. Appl. Phys. 87, 1769 (2000).

[15] T.E. Jenkins J. Phys. C: Solid State Physics 19, 1065 (1986).

[16] D.E. McCumber, and M.D. Sturge J. Appl. Phys. 34, 1682 (1963).

[17] V. Lupei, A.Lupei, and G. Boulon, Phys. Rev. B 53(22), 14818-26 (1996)

[18] V. Lupei, A.Lupei, and G. Boulon,, J. of Luminescence 72-74, 948-950 (1997)

CHAPTER 4

Experimental results: YAG-YSGG mixed garnets

4.1 *Vibrational properties of mixed (YAG)$_x$ - (YSGG)$_{1-x}$ crystals.*

4.1.1. Experimental setup and growth condition of analyzed samples

Analyzed samples with $(Y_3Al_5O_{12})_x$-$(Y_3Sc_2Ga_3O_{12})_{1-x}$ mixed structure, doped with 1% at. of Nd, were grown in the growth laboratory of Scientific Materials Europe (Italy) by Czochralski method.

The stoichiometric term x was used as a simplification of the formula $Y_3Al_{(2-y)}Sc_yAl_{(3-z)}Ga_zO_{12}$ and it represents the relative concentration of Al, Sc and Ga in the melt. The stoichiometric composition of samples was controlled by changing the amount of Ga_2O_3 and Sc_2O_3 oxides in the melt in order to obtain the desired relative concentration of YAG and YSGG. Table IX summarizes the compositional structure of analyzed samples. Prime oxides of Al_2O_3, Y_2O_3, Ga_2O_3 and Sc_2O_3 (all with 99.999% purity) were mixed and pre-sintered under pressure of 140 MPa and processed at 1400°C for 24 hours. Sintered tablets, with first composition of $YAG_{0.55}YSGG_{0.45}$, were melted at 1970 °C in iridium crucible and pulled at 0.8 mm/h with ω_r=15 rpm in Ar atmosphere. The obtained undoped boule was used as a seed for pulling Nd-doped melt.

Sample	**YAG(1-x)**	**YSGG(x)**
Pure YAG	1.000	0.000
A	0.550	0.450
B	0.520	0.480
C	0.470	0.530
D	0.423	0.577
E	0.416	0.584
F	0.412	0.598
G	0.399	0.601
Pure YSGG	0.000	1.000

Table IX: *Compositional structure of analyzed samples*

Raman scattering measurements were carried out in back scattering geometry along the [111] crystal direction by using the 514.5 nm line of an Argon-ion laser. Measurements were performed in air at room temperature with a triple spectrometer Jobin-Yvonne Dilor integrated system with a spectral resolution of about 1 cm^{-1}. Spectra have been recorded in the Stokes region by a 1200 grooves/mm grating monochromator and a CCD detector system.

4.1.2. Results and discussion

As said before the crystal structure of Yttrium Aluminium Garnets (YAG) belongs to a body centred cubic, O_h^{10} –Ia_3d, with eight formula units in the primitive cell [1-6]. 24 Aluminium atoms are tetrahedrally coordinated to oxygen atoms while the remaining sixteen Al atoms are coordinated to the O atoms with an octahedral symmetry [6].

A factor group analysis of the YAG structure shows that there are 98 vibrational modes at **k**=0 belonging to the following irreducible representation:

$$5A_{1u} + 3A_{1g} + 5A_{2u} + 5A_{2g} + 10E_u + 8E_g + 14T_{1g} + 18T_{1u} + 14T_{2g} + 16T_{2u}$$

where the A_{1g}, E_g and T_{2g} modes are Raman active, the T_{1u} modes IR- active, and the others silent [6]. In Figure 4.1 the Raman spectrum of YAG crystal in the 200-1000 cm^{-1} range is presented; the main peaks can be easily identified and assigned according to Hurrell et al. (Table X)[6].

The Raman spectrum of the YSGG crystal is also reported in Figure 4.1 and the peak positions in the 200-1000 cm^{-1} range are listed in Table X with the proposed attribution according to the discussion reported below.

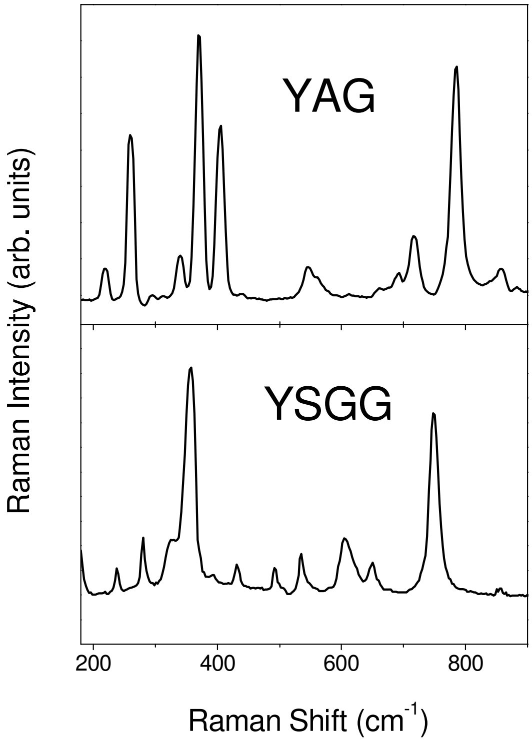

Fig. 4.1: *Raman spectra of pure YAG and YSGG single crystals.*

Vibrational mode	YAG	YSGG
E_g	161	179
T_{2g}	219	237
T_{2g}	261	279
E_g	339	unresolved
A_{1g}	372	
E_g	403	
E_g	530	394
T_{2g}	545	430
A_{1g}	560	492
T_{2g}	690	536
T_{2g}	714	604
T_{2g}	720	650
A_{1g}	785	752

Table X: *Raman frequencies and relative assignments in YAG and YSGG single crystals.*

The YSGG crystal is characterized by the body centred cubic symmetry and the vibrational modes at **k**=0 belong to the same irreducible representation reported for the YAG crystal. The YSGG structure can be obtained from the YAG structure by substitution of Aluminium 2+ ions at the octahedral sites with Scandium ions and by substitution of Aluminium 3+ ions at the tetrahedral sites with Gallium ions [1,7].

It has been reported that the vibrational spectrum of YAG crystals can be interpreted on the basis of characteristic vibrations of the AlO_4 tetrahedral and AlO_6 octahedral sites [6,8-10]. According to this interpretation, the Raman spectrum can be divided in three different parts: the bands in the 400-600 cm^{-1} range are related to the vibrations of Al-O in quasi-isolated AlO_6 octahedral sites while the peaks between 600 and 800 cm^{-1} belong to vibrations of Al-O in quasi-isolated AlO_4 tetrahedral. On the contrary the Raman bands in the low wave numbers region are related to the motions of the cations with respect to the whole structure [6,8,9].

The proposed interpretation is based on the comparison with the vibrational frequencies of a number of molecules and allows to describe the oxygen vibrations in the high frequency range while those in the low wave numbers region are strongly mixed to the vibrations of the cations and cannot be interpreted by means of vibrations of specific structures [6,8-11]. Taking into account this model, Raman modes of the YSGG structure can be assigned on the basis of the specific vibrations of the YAG crystal.

The symmetric stretching mode (A_{1g}), due to the isolated octahedron in YAG crystal, is reported at 560 cm^{-1}, while the E_g and T_{2g} vibrations are detected at 530 and 545 cm^{-1}, respectively. By substituting the central cation with a heavier and larger atom a shift of the octahedral vibrational modes to lower wavenumbers is expected. As already reported for the free polyhedra structure [12], the shift is not rigid, it is larger for the T_{2g} mode than for the A_{1g} mode and a larger separation of the two bands in the YSGG Raman spectrum can be observed.

Thus we propose to assign the vibrations at 492 and 430 cm^{-1} in the YSGG Raman spectrum to the T_{2g} and A_{1g} modes respectively. Concerning the E_g mode its intensity is very low in both the investigated structures and a shift from 530 cm^{-1} in the YAG crystal to 394 cm^{-1} in the YSGG can be hypothesized.

As regards the three vibrations at 339, 372, and 403 cm^{-1} detected in YAG crystals, their counterparts can be tentatively identified in the composite vibrational structure peaked at 358 cm^{-1} with a shoulder at 327 cm^{-1}. It has been reported that the 372 cm^{-1} mode corresponds to the rotational vibration of the AlO_4 units in the YAG structure around two perpendicular axes, while the octahedra vibrate in a similar way around another set of perpendicular axes[9].

The vibrations at 403 and 339 cm^{-1} possess the E_g symmetry but cannot be ascribed to the vibrations of an isolated structure (tetrahedron or octahedron). As deduced from the partial phonon density of the YAG structure, calculated by Papagelis et al. [10], the contributions of isolated tetrahedron and octahedron overlap within this spectral region. The substitution of the central cation with a heavier atom causes a blue shift of the vibrational modes of the two isolated structures.

Thus in the Raman spectrum of the YSGG the bands overlap leading to the composite vibrational structure peaked at 358 cm^{-1} with a shoulder at 327 cm^{-1}.

Concerning the low frequency modes (< 300 cm^{-1}) of the Raman spectrum of the YAG crystal, they are associated to mixed modes due to the coupling between octahedral and tetrahedral structures in the garnet crystal [6,9,11]. It has been reported that the low wavenumber modes blue-shift while increasing the unit cell dimensions in Rare-Earth doped aluminium garnets [9]. The lattice constant of the YAG structure is 12.01 Å and it increases to 12.45 Å in the YSGG garnet crystal [13,14]. Thus the bands at 179, 237 and 279 cm^{-1} in the Raman spectrum of the YSGG garnet structure correspond to the vibrations found at 161, 219 and 261 cm^{-1} in the YAG Raman spectrum and share the same attribution.

In addition, the increase of the unit cell dimensions and the substitution of the Al^{3+} ions with Ga ions generate a red-shift in the vibrations modes associated to the tetrahedral sites (> 650 cm^{-1}) [10,11]. The modes at 690, 714, 720 (T_{2g}) and 785 cm^{-1} (A_{1g}) in the YAG structure red-shift to 536, 604, 650 and 752 cm^{-1} respectively in the YSGG. As already discussed indeed the A_{1g} mode of the free tetrahedron presents a downshift lower than the T_{2g} mode when the cation is replaced with a heavier ion [12].

The Raman spectra of different mixed garnet crystals ($YAG_x/YSGG_{1-x}$) are reported in Figure 4.2.

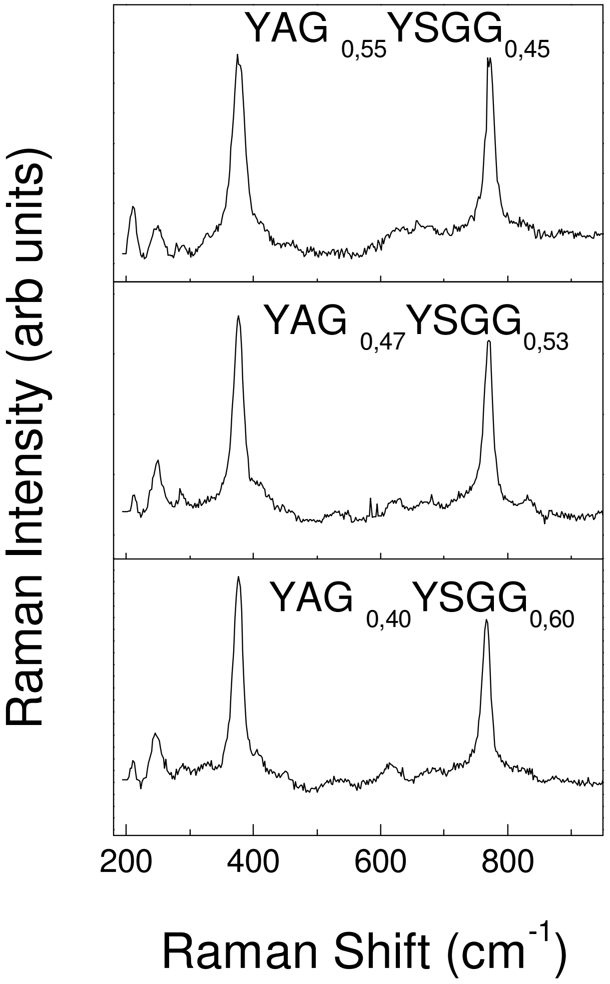

Fig. 4.2: *Raman spectra of mixed garnet crystals (*$YAG_x/YSGG_{1-x}$*).*

The main variations with the increase of the YSGG relative concentration can be observed in the Raman peaks between 650 and 800 cm^{-1} where a progressive red-shift of the peaks is detected. On the contrary, the vibrational modes at about 400 cm^{-1} are less affected by the variation of the relative concentration of the two garnets. The Raman bands of the mixed samples show a larger width than the bands of pure YAG and YSGG crystals. However, the spectrum does not show the presence of new vibrational bands. In order to verify this hypothesis, the Raman spectra of mixed garnets were fitted with lorentzian bands by means of a least-square fit procedure.

As an example, the deconvolution of the Raman spectrum of the $YAG_x/YSGG_{1-x}$ (x = 0.55) sample is reported in Figure 4.3.

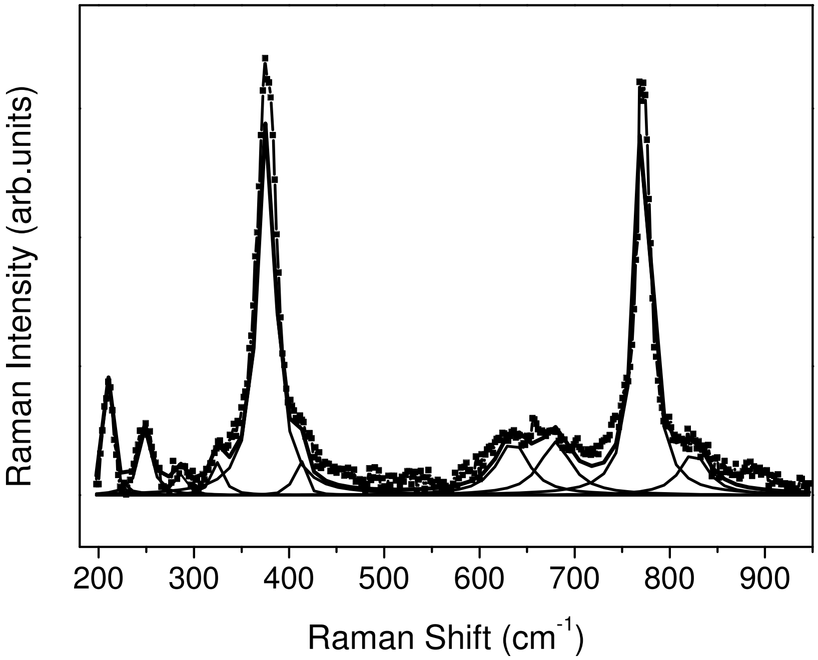

Fig. 4.3: *Deconvolution of the Raman spectrum of* $YAG_{0.55}YSGG_{0.45}$ *mixed garnet.*

The fitting procedure was carried out by introducing the same number of bands observed in both the YAG and YSGG Raman spectra. The peak positions of the vibrational modes of the mixed garnets lye between the positions of the corresponding bands of the single crystals. The good agreement between the fitting procedure and the experimental data (square correlation factor $R^2 \geq 0.99$) allows to confirm the substitutional role of Sc and Ga ions in the mixed garnets and that the symmetry of the structure is preserved. The Raman spectra of mixed garnets show that the Raman bands in the central part of the spectra present a partial or total overlapping of the different vibration modes, making difficult a systematic study of the Raman shift as a function of the variation of the relative concentration of the two garnets. Further measurements, at low temperature condition and with higher resolution can be performed in order to better analyze the behavior of these vibration modes. On the contrary, the non degenerated A_{1g} mode (the breathing of the free tetrahedral molecule) is very intense and does not overlap with other Raman bands, allowing for a detailed analysis of its Raman shift as a function of the mixed garnet composition. Due to the large cation-anion bonding interaction in the garnet structure, the analysis was carried out in the framework of the free tetrahedron model [6,10,11].

In principle the analysis could be performed upon the modes related to isolated octahedron. However the low intensity of these modes does not allow to precisely identify them in the garnet structures. On the contrary the vibrational modes in the 400 cm^{-1} range (at 339, 372 e 403 cm^{-1} in the pure YAG) display a larger intensity but cannot be interpreted in the framework of the single molecule model. Indeed the spectrum of the phonon dispersion in this spectral region indicates the overlapping of the octahedron and tetrahedron structures preventing the analysis with a single molecule model [9].

The application of the model to the analysis of the A_{1g} Raman shift as a function of the relative concentration of the YSGG structure is supported by the observation of the A_{1g} stretching mode of tetrahedral sites in YSGG crystal at 752 cm^{-1}, very close to the vibration frequency of the same mode in Yttrium Gallium Garnet (YGG) single crystal (758 cm^{-1}) [15,16].

Indeed YSGG and YGG crystals have the same crystal symmetry with gallium atoms located in the tetrahedral positions in both the crystals while the occupancy of the central anions in the octahedral sites is different (Gallium in YGG, Scandium in YSGG). Thus, the tetrahedral vibration modes are slightly influenced by the neighbouring atoms and the free tetrahedron model can be applied. The A_{1g} mode is at 783 cm^{-1} in the Raman spectrum of the YAG crystal and progressively downshifts as the relative concentration of YSGG in mixed garnets increases. In the pure YSGG crystal the A_{1g} mode is at 752 cm^{-1}. In Figure 4.4 the peak position of the A_{1g} mode for different mixed crystals is reported as a function of the relative concentration of YSGG garnet. In order to study the shift of the A_{1g} mode the variation of the potential in the free tetrahedral structure was investigated according to the rigid ion model [10].

The rigid ion model can explain the motion of the atoms in the garnet structure and allows to calculate the frequencies of the Raman active modes. In this model, the atoms are considered as charged points which interact via short and long-range forces. The potential affecting the motion of the atoms and the frequency of the total symmetric stretching mode in the mixed crystals is calculated starting from the potential in the pure YAG and YSGG structures.

The Born-Mayer potential was applied to model the short range repulsive interaction potential [10,17]. The potential is of the form

$$V^{SR}\left(\left|\mathbf{r}(lk)\right| - \left|\mathbf{r}(l'k')\right|\right) = V_0 e^{\frac{\left|\mathbf{r}(lk)\right| - \left|\mathbf{r}(l'k')\right|}{\sigma_k + \sigma_{k'}}} , \qquad (4.1)$$

where $\mathbf{r}(lk)$ is the position vector of the k atom in l-th primitive cell, V_0 and $\sigma_k+\sigma_{k'}$ are the parameters describing the strength and the range of the repulsive interaction, respectively. The potential depends on the distance between the central atom and the nearest neighbors. Some vibrational motions in the garnet structure can be described like the sum of the singular motion of each polyhedron [10]. For example in the YAG composition, the vibrational frequency at 785 cm^{-1} of the A_{1g} vibrational mode can be considered as due to the motion of free tetrahedra.

In the approximation of free tetrahedron for the A_{1g} vibration mode, it is possible to consider only the motion of the oxygen atoms with respect to the central cation; a simplified form of the potential of the pure YAG or YSGG crystal [17] is:

$$V_{cryst} = \sum_j A_{O-j} e^{-b_{O-j} r_{O-j}} \tag{4.2}$$

where the terms A_{O-j} and b_{O-j} represent the strength and the range of the repulsive interaction between the oxygen and the other atoms of the tetrahedron, respectively. For a given pair of atoms, A_{O-j} and b_{O-j} are constant values and can be calculated from the single atom parameters [17]: $A_{O-j} = (A_j A_O)^{1/2}$ and $b_{O-j}=(b_j + b_O)/2$.

By using the harmonic approximation, this potential can be applied to calculate the vibrational frequencies of the breathing mode of a free tetrahedron. Starting from the values reported by Abrahamson [17] for the interaction of free atoms, the parameters for the ions constituting the YAG and YSGG structures were calculated by fitting the A_{1g} symmetric stretching in the two garnets.

In the rigid ion model framework the atoms can be considered as charged point interacting with short range forces, where the force constant is related to the second derivative of the potential:

$$k = \frac{d^2 V_{cryst}(r)}{dr^2} \tag{4.3}$$

By using the expression (4.2) for the Born Mayer potential and the harmonic approximation to fit the frequency of the A_{1g} stretching mode the A_{O-j} and b_{O-j} parameters were calculated for the YAG and YSGG garnet structures. The obtained values are b_{O-Al}= 3.0 Å^{-1} and b_{O-Ga}= 2.4 Å^{-1} and 736 eV and 1520 eV for A_{O-Al} and A_{O-Ga} respectively. It can be noted that the parameters calculated by Abrahamson for the free atoms are larger than the values here calculated: indeed in the present model the atoms are not free but linked in the tetrahedral structure.

In addition one should consider that the position of the A_{1g} stretching mode is fitted by assuming the tetrahedron as isolated while it is linked into the garnet structure.

As previously discussed, the mixed crystal is realized by gradually substituting the Al cations of YAG structure with the Sc and Ga cations of the YSGG, without changing the crystalline structure and the unit cell symmetry. Then it can be hypothesized that the interaction potential for the mixed garnet can be expressed as a linear combination of the interaction potentials of the two separated phases. The obtained parameters $b_{O\text{-}j}$ and $A_{O\text{-}j}$ were used to calculate the A_{1g} frequency in the mixed garnets as a function of the relative concentration of the two compounds (Figure 4.4):

$$V_{mix} = (cA^0_{YAG} + (1-c)A^0_{YSGG})e^{-(cb_{YAG}+(1-c)b_{YSGG})(cr_{YAG}+(1-c)r_{YSGG})} \tag{4.4}$$

where c ($0<c<1$) is the relative concentration of the YAG phase in the mixed structures.

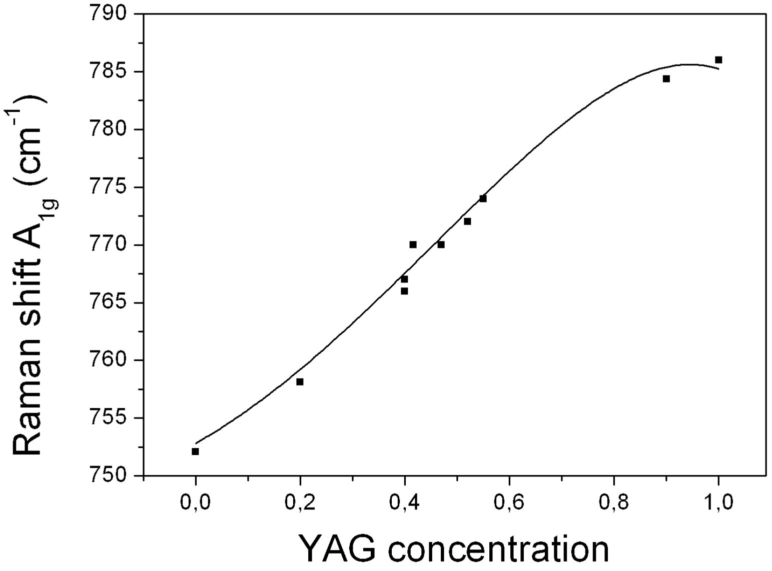

Fig. 4.4: *Experimental data of the Raman position of the A_{1g} vibrational mode vs YAG relative concentration in the mixed garnet. The solid line represent the theoretical curve.*

The very good agreement between the experimental data and the theoretical curve reported in Figure 4.4 indicates that the proposed free tetrahedron model is able to represent both the single and mixed structures allowing to predict the A_{1g} frequency for a given relative concentration of the garnets.

4.2 Compositional tuning of photoluminescence properties in Nd-doped YAG-YSGG mixed structures

4.2.1. Experimental setup

Photoluminescence measurements were performed with a single-pass spectrometer (Dilor XY800). An argon ion laser operating at 514.5 nm (Coherent Innova 90C-4) provided the excitation. The signal, dispersed with a 600 grooves/mm grating, was detected by a 1024 x 256 LN2 cooled charge coupled detector (CCD). All PL measurements were performed at room temperature with a spectral resolution of 0.1 nm.

4.2.2. Results and discussion

In Figure 4.5 the PL spectrum of Nd:YAG in the 860-950 nm range is compared with the spectra of samples with mixed composition (see Table XI).

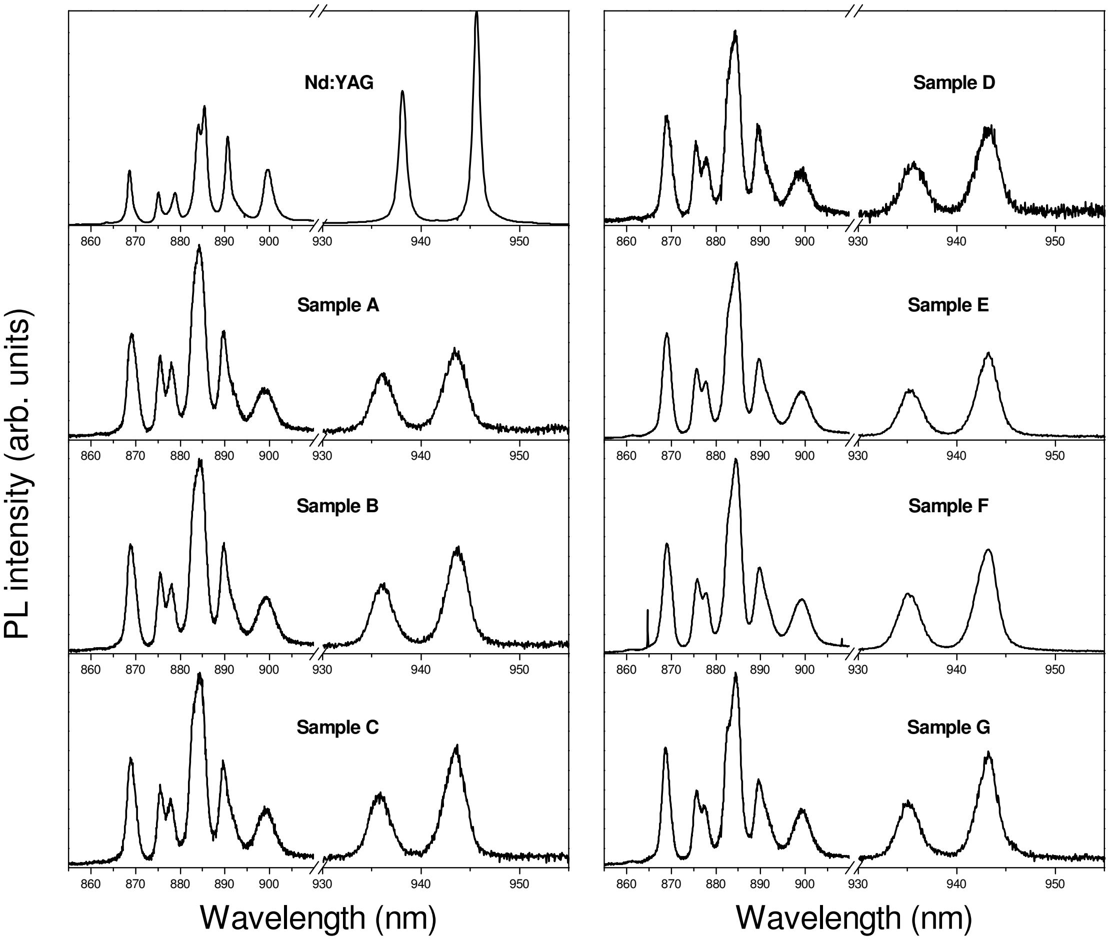

Fig.4.5: *Photoluminescence spectra of Nd:YAG and Nd:YAG$_x$YSGG$_{1-x}$ mixed garnet at different ratios YSGG/YAG.*

Sample	**YAG(1-x)**	**YSGG(x)**	**$R_1 \rightarrow Z_5$** ***Peak position (eV)***	***FWHM (meV)***	**Voigt shape S_v**
Pure YAG	1.000	0.000	1.3106	1.2286	1.7400
Ref.[23]	0.750	0.250	1.3120	3.3061	0.34320
Ref.[23]	0.667	0.333	1.3128	3.5746	0.26710
Ref.[23]	0.600	0.400	1.3140	3.8537	0.23030
A	0.550	0.450	1.3139	3.8315	0.42545
B	0.520	0.480	1.3138	3.7639	0.46330
C	0.470	0.530	1.3142	3.8549	0.44055
D	0.423	0.577	1.3145	3.8509	0.40225
E	0.416	0.584	1.3145	3.8723	0.36993
F	0.412	0.598	1.3146	3.7285	0.40306
G	0.399	0.601	1.3147	3.6391	0.42119
Pure YSGG Ref.[23]	0.000	1.000	1.3211	2.0060	0.66666

Table XI: *Relative material compositions and results of Voigt profile fitting. Entries belonging to pure YAG and samples A through G were analyzed in this work, while the remaining entries belong to samples from reference [23].*

It is worth noting that the emissions in mixed structures can not be related to separate contributions of Nd:YAG and Nd:YSGG [27], excluding the presence of separated phases of different garnets. Due to the broadening and the overlapping of the PL bands in the 860-920 nm region the analysis of the PL modifications, as the relative concentration of YSGG in the mixed structure increases, was performed on the luminescence peaks at 946 nm and 938 nm. Further measurements, at low temperature condition and with higher resolution, can be performed in order to better analyze the behavior of this spectral region.

It is well known that the observed bands in Nd:YAG in the 860-950 nm range involve the R_1-R_2 stark components of the $^4F_{3/2}$ manifold and the Z_1-Z_5 stark components of the fundamental level $^4I_{9/2}$ [18]. The R_1-Z_5 and R_2-Z_5 transitions (946 nm, 938.5 nm) of Nd:YAG were considered as references to estimate the wavelength shift and band broadening of the analyzed samples as a function of YSGG concentration (Figure 4.6).

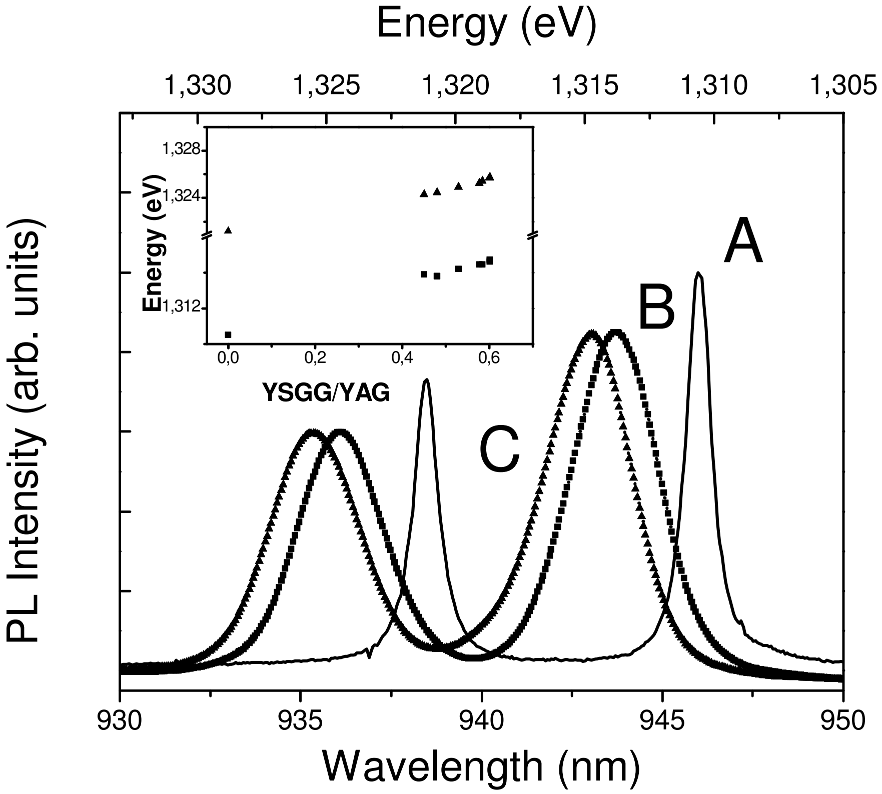

Fig.4.6: *Photoluminescence spectra of* R_1-Z_5 *and* R_2-Z_5 *transitions in different samples: A) Nd:YAG; B) Nd:*$YAG_{0.520}YSGG_{0.480}$*; C) Nd:*$YAG_{0.400}YSGG_{0.600}$*. Inset: peak position of the* R_1-Z_5*,* R_2-Z_5 *transitions as a function of the doping ratio*

It can be observed that the compositional variation of the host materials shifts towards the blue region the Nd^{3+} emission bands of about 3 nm as summarized in Table XI. In addition, the full width at half maximum (FWHM) of the analyzed bands increases as the YSGG relative concentration approaches 0.5; above this threshold the PL-FWHM decreases as the YSGG relative concentration increases (Table XI). The inset of Figure 4.6 shows the variation of the peak position for the R_1-Z_5 and R_2-Z_5 transitions as a function of the doping process:

the rigid blue-shift of both emissions, at least within the experimental error, allows to hypothesize that the compositional tuning is related to the variation of the energy position of the ground level Z_5.

The luminescence properties of Nd^{3+} ions in YAG host in the range between 750 nm and 1100 nm are well known. In this region the emission bands are due to the transitions between R_1 and R_2 stark components of the $^4F_{3/2}$ level and the Z_1-Z_5 stark components of the fundamental level $^4I_{9/2}$ or to the Y_1-Y_6 stark components of the $^4I_{11/2}$ level [28]. The PL spectrum of Nd:YAG in the spectral range 860-910 nm is compared to that of a mixed-structure sample (sample A in Table XI) on Figure 4.7.

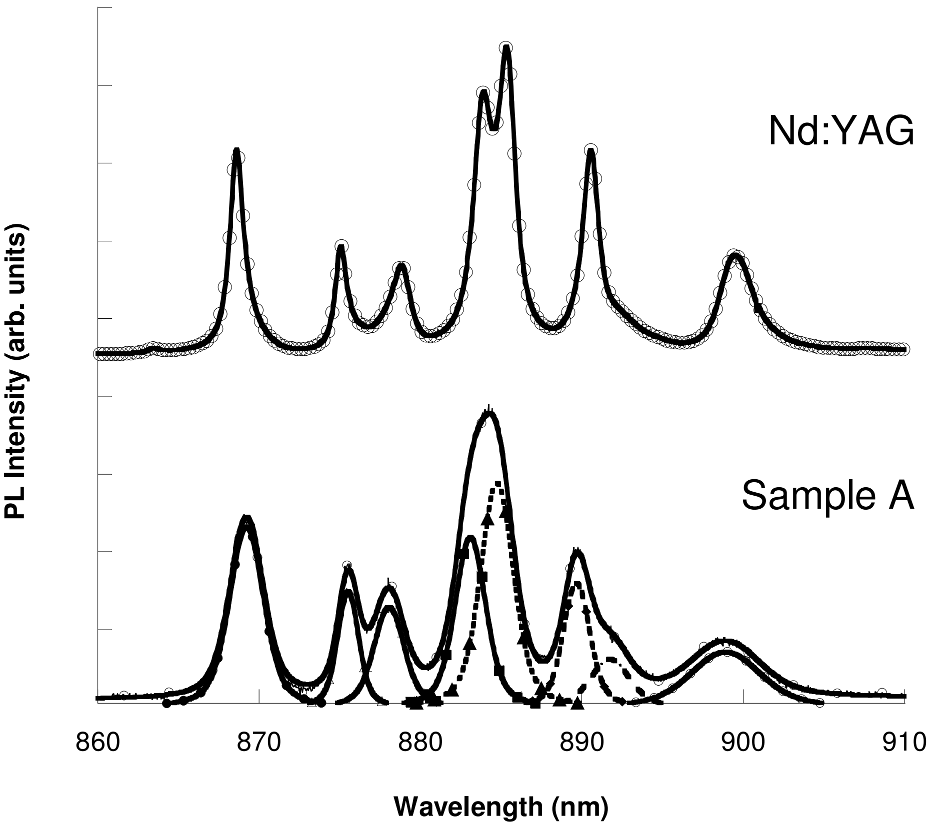

Fig.4.7: *PL spectrum of Nd:YAG and of the Nd:YAG$_{0.550}$YSGG$_{0.450}$ mixed garnet (sample A). The spectrum of the sample A was deconvoluted by means of Voigt profiles.*

The spectrum of sample A was deconvoluted by means of Voigt profiles, assuming the spectral properties of the Nd:YAG sample as references. The fitting curve reproduces very well the experimental data, confirming the previously discussed mixed nature of the investigated structures. Voigt profiles of the emission bands were chosen because of the mixed contribution of homogeneous and inhomogeneous broadening of the spectral lines.

It is well known that a physical process that has the same probability of occurrence for all the atoms in the system produces a Lorentzian line shape (homogeneous broadening), while a physical process that has a random distribution of occurrence for each atom produces a Gaussian line shape (inhomogeneous broadening). If both types of broadening processes are present, the line shape is the convolution of Lorentzian and Gaussian contributions represented by a Voigt profile. The emission processes due to Nd^{3+} levels in garnet structures strongly depend on the neighbor atoms and their contribution to the local crystalline field [23,29], suggesting the Voigt profile choice.

The fitting procedure was successfully carried out on the R_1-Z_5 and R_2-Z_5 transitions of each sample. Fitting parameters are reported in Table I. Figure 4.8 shows the Voigt profile FWHM of the R_1-Z_5 transition as a function of the YSGG relative concentration. The variation of the Voigt width indicates that the Gaussian and Lorentzian components, that is the homogeneous and inhomogeneous broadening, depend on the YSGG concentration.

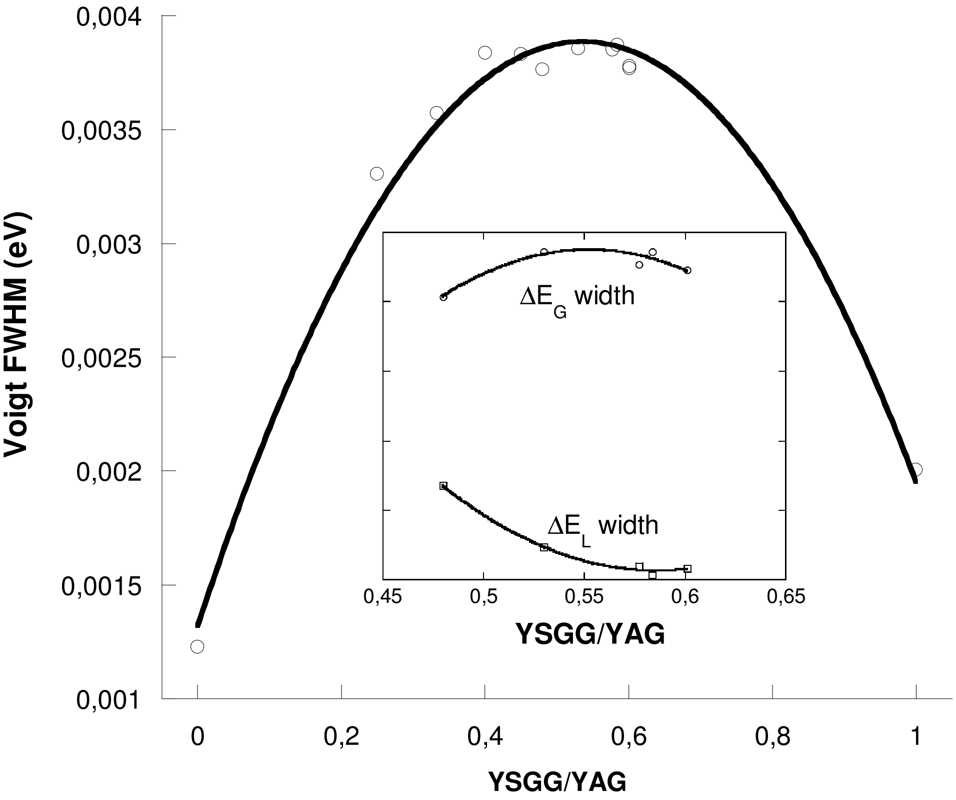

Fig.4.8: *Voigt profile FWHM of the* R_1*-*Z_5 *transition as function of the YSGG relative concentration in the mixed garnet. The inset reports the widths of the Lorentzian (*ΔE_L*) and Gaussian (*ΔE_G*) component of the Voigt profile as a function of the YSGG relative concentration.*

As reported in Figure 4.8 the FWHM shows a maximum at 50% of YSGG relative concentration. In these conditions half of the Y^{3+} sites of the elementary cells belongs to the YSGG structure (A sites) and the other half belongs to the YAG structure (B sites). The dopant ions have a 50% probability to occupy both sites, causing the largest inhomogeneous broadening. If the YAG structure is predominant, the probability to occupy B sites is higher, causing a decrease of FWHM because of the larger contribution of homogeneous behavior. The analysis is confirmed by the variation of the Gaussian and Lorentzian widths, ΔE_G and

ΔE_L, as functions of the YSGG relative concentration (see the inset on Figure 4.8). The Gaussian width increases with the increase of YSGG relative concentration and reaches a maximum when the relative concentration of YSGG is 0.5. On the contrary, the Lorentzian width decreases with increasing the YSGG relative concentration and shows a minimum at the Gaussian width maximum. The analysis of the Voigt shape parameter, S_v, defining the relative weight of a Lorentzian contribution to the linewidth with respect to a Gaussian one [23], is a further confirmation of the just discussed broadening trend. The equation describing the Voigt shape S_v is given as:

$$S_v = \frac{1}{\sqrt{ln(2)}} \frac{\Delta E_L}{\Delta E_G} \qquad (4.5)$$

indicating the predominance of Gaussian ($S_v < 1$) or Lorentzian ($S_v > 1$) nature of the emission band. The calculated S_v parameters are reported in Table I.

As shown in the Figures 4.5 and 4.6, and as previously discussed, the observed emission bands are related to the transitions of Nd^{3+} ions hosted in the mixed garnet structure. The number of the stark components reported in the spectra is in good agreement with the group theory and the stark effect analyzed by Kaminski and Powell in Nd:YAG [27,29]. As indicated in the Eq. 3.1 the Hamiltonian of an ion in a crystal field is given by the sum between different terms that indicate the interaction of each electron with the nucleus (H_0) and other three terms treated as successive perturbations. These describe the Coulomb interaction of the electrons with each other (H_e), the spin-orbit interaction (H_{SO}), and the interaction of the electron with the crystal field of the ligands (H_c). As illustrated in Chapter 3, in the case of Nd^{3+} ions (shielded *f*-electrons), the perturbations can be treated in the weak-field approximation where the strength of the crystal field is smaller than the Coulomb interaction of the electrons with each other and the spin-orbit coupling interaction ($H_c<H_{SO}$, H_e) [27,29].

The Stark splitting is due to the local symmetry of the activator center related to the structure of the host material, while the number of Stark components depends on the quantum number **J** in the weak-field approximation (see Table VIII). As said before the unit cell of garnet structure is composed of eight molecules of $P_3Q_2(RO_4)_3$ [30]. Cations P, Q, and R have respectively 8, 6, and 4 nearest neighbor oxygens, and are situated at the 24*c*, 16*a*, and 24*d* Wyckoff positions in the unit cell [30].

The Yttrium ions occupy the *c* sites and are surrounded by eight oxygen ions in the shape of a distorted cube. The Nd^{3+} ions occupy Y^{3+} sites in YAG and YSGG as isovalent substitutional defects. The *c* site local symmetry is D_2 and the Stark components related to this center, for an electron in nf^3 configuration, are two and five for J=3/2 and J=9/2, respectively [27,29]. As previously discussed, the deconvolution of the PL bands in samples with different YSGG relative concentration can be successfully performed assuming the PL spectrum of Nd:YAG as a reference.

Thus, we can hypothesize that the symmetry related to the Nd^{3+} ions in these samples is the same as that of the *c* sites in garnets with D_2 symmetry and that it does not change as the YSGG concentration increases. Therefore, the shift of the PL bands can be interpreted by a variation of the crystalline field due to modifications of the reticular parameters associated with the presence of Sc and Ga atoms in *a* and *d* sites.

As previously discussed in Chapter 3, in the case of D_2 symmetry, the term H_c, that describes the crystalline field contribution in (3.1), can be expressed by expanding the crystalline field potential with spherical harmonics [29] as proposed in the Eq. (3.2) and (3.3) where the *i* and *j* subscript indicates the optical electrons of Ze-charged ligand ions considered as point charges. In (3.3) the A_{lm} are expansion coefficients that depend on the specific lattice structure giving rise to the local crystal field, while the term $R_l(r)$ is the radial function of the system. In addition the Eq. 3.4 explicitates the term A_{lm} and $R_l(r)$ in the case of D_2 symmetry.

By assuming that the progressive introduction of Ga and Sc atoms in YAG elementary cell affects the crystalline field term in (3.1), the energy eigenvalues of (3.1) can be expressed as:

$$E = E_0 + \Delta E_c \qquad (4.6)$$

where the term E_0 indicates the "unperturbed" energy eigenvalues before the introduction of Sc and Ga atoms and ΔE_c indicates the energy variation due to the V_c modification after their introduction. The energy variation can be expressed in differential form as:

$$d\varepsilon_c = dV_c(s,\theta,\varphi) = \frac{\partial V_c}{\partial s} ds + \frac{\partial V_c}{\partial \theta} d\theta + \frac{\partial V_c}{\partial \varphi} d\varphi \qquad (4.7)$$

As previously discussed, Sc and Ga atoms, occupy a and d sites in garnet structure. The progressive introduction of Sc and Ga atoms changes the dimensions of the coordination polyhedra modifying the mixed garnet lattice parameters without changing the coordination symmetry of *c* sites. Because of unchanged c site symmetry, the modification of lattice parameters can be ascribed to a variation of the s distance, leading to the following expression for the energy variation:

$$\frac{d\varepsilon_c}{ds} = \frac{dV_c}{ds} \qquad (4.8)$$

By introducing the crystalline field expressed in (3.3) and (3.4) one obtains:

$$\frac{d\varepsilon_c}{ds} = \sum_l \sum_m A_{lm} Y_l^m \frac{r^l}{-(l+1)s^{l+2}} = \sum_l \frac{r^l}{-(l+1)s^{l+2}} \sum_m A_{lm} Y_l^m = \sum_l B_{lm} \frac{r^l}{s^{l+2}}$$

(4.9)

where B_{lm} and r^l are constants. The B_l coefficients derive from the expression:

$$B_{lm} = -\frac{\sum_{m} A_{lm} Y_l^m}{(l+1)} \qquad (4.10)$$

where $A_{lm}Y_l^m$ are independents from the *s* distance. Moreover the *s* distance does not depend upon a specific oxygen atom, thus it is independent from the sum over the *m* subscript. If the proposed model is applied to the *f* electrons of Nd^{3+}, equation (3.1) can be solved for even values of the *l* quantum number with upper value of 6 [29]. The resulting expression can be used to fit the energy shift of the peak position of the emission bands as a function of the *s* distance. The latter can be finally related to the relative concentration of YSGG in the mixed structure.

Indeed, by means of a computer simulation of the YAG and YSGG pure structure the s distance can be evaluated in the pure garnets. By assuming the value of 12.01 Å and 12.45 Å for the reticular constant of YAG and YSGG [27,29] the s distance is 2.5 Å and 2.7 Å in YAG and YSGG hosts respectively. Then, it can be deduced that the s distance increases as the YSGG relative concentration increases. As previously discussed, the mixed structure is realized by gradually substituting the Al cations of YAG structure with the Sc and Ga cations of the YSGG, without changing the crystalline structure and the unit cell symmetry. Thus, in the mixed structure the s distance can be expressed as a linear combination of the values in the pure garnets:

$$s = Cf' + (1-C)f'' \qquad (4.11)$$

where the terms f' and f'' represent the Y-O distance in YSGG and YAG respectively and *C* is the relative concentration of YSGG. In Figure 4.9 the fitting procedure is successfully applied to the experimental data: the shift of the peak position of the PL band due to the R_1-Z_5 transition is fitted by using equation (4.9) with the *s* distance given by (4.11).

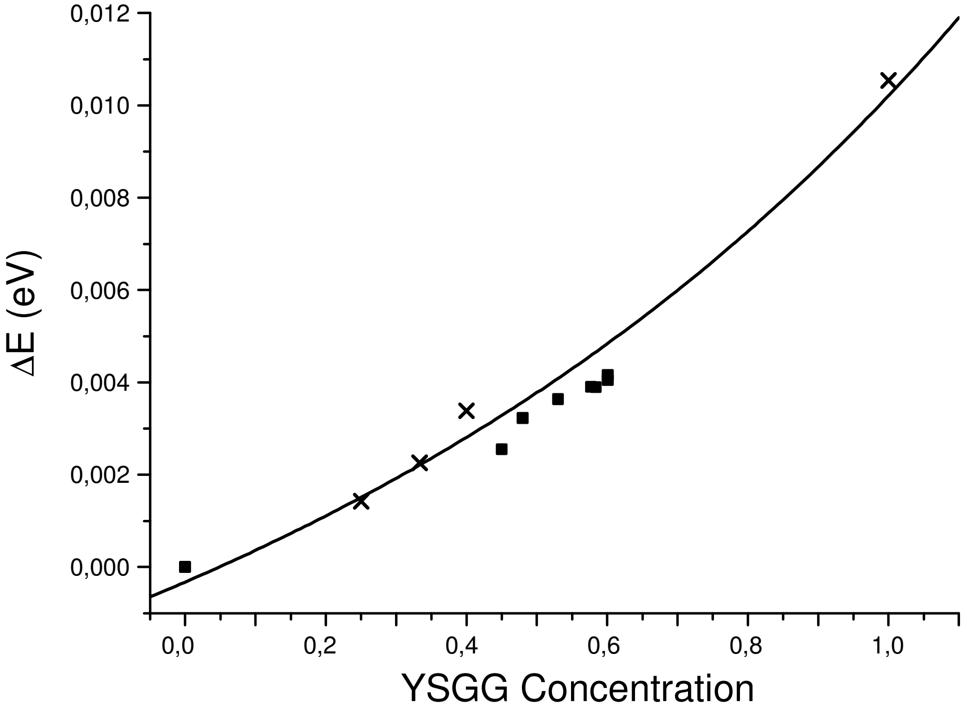

Fig.4.9: *Fitting procedure applied to the photoluminescence peak shift of R_1-Z_5 Neodymium transition as a function of YSGG relative concentration in the mixed garnet (■ this work; × ref. [23]).*

The very good agreement between the analytical model and experimental data allows us to predict the effect of compositional tuning in mixed garnet structures.

References

[1] B.M. Walsh, N.P. Barnes, R.L. Hutchenson, R. W. Equall and B. Di Bartolo, J.opt. Soc. Am. B 15, 2794 (1998)
[2] B.M. Walsh, N.P. Barnes, R.L. Hutchenson and R. W. Equall, IEEE Journal of Quantum electronics 37, 1203 (2001)
[3] R. Treichel, C. Czeranowsky, B. Ileri, K. Petermann, G. Huber European Space Agency, (Special Publication) ESA SP 554, 639 (2004)
[4] N.P. Barnes, B.M. Walsh and R.L. Hutchenson, Advanced Solid State Laser 1, 522 (1996)
[5] W.B. Grant, "*Lidar for atmospheric and hydrospheric studies*" in Tunable Laser Application, F.J. Duarte, Ed. New York: Marcel Dekker 1995, p.241
[6] J.P. Hurrel, P.S. Porto, I.F. Chang, S.S. Mitra R. P. Bauman Phys. Rev. 173, 851 (1968)
[7] J.B. Gruber, M.E. Hills, T.H. Allik, C.K. Jayasankar, John R. Quagliano and F.S. Richardson, Phys. Rev. B 41, 7999 (1990)
[8] M.Thirumavalavan, J.Kumar, F.D.Gnanam, P.Ramasamy Infrared Phys. Vol.26 101(1986)
[9] K. Papagelis, S. Vrs J. Appl. Phys 94 6491 (2003)
[10] K.Papagelis G. Kanellis S. Ves G.A Kourouklis Phys. Stat. sol. 233 134 (2002)
[11] K.Papagelis G. Kanellis, J. Arvanitidis, G.A Kourouklis S. Ves Phys. Stat. sol. 215 193 (1999)
[12] K. Nakamoto*, "Infrared and Raman spectra of Inorganic and coordination Compounds" ,* J. Wiley, Ed. New York (1997)
[13] A.A. Kaminskii, *"Laser Crystals- Their physics and Properties" Springer, New York 1981*
[14] R. C. Powell, *"Physics of Solid State Laser Materials"* AIP Press Springer, 1998
[15] J. A. Koningstein O.S. Mortensen J. Molecular Spectr. 27, 343 (1968)
[16] A. M Hofmeister, K.R. Campbell J. Appl. Phys. 638 (1992)
[17] A. A. Abrahamson Phys. Rev. 178, 76 (1969)
[18] W. Koechner, "Solid-State Laser Engineering", Springer-Verlag, Berlin 1996
[19] G. S. Pomrenke, P. B. Klein and D. W. Langer "Rare Earth Doped Semiconductors" MRS Pittsburg 1993
[20] V. Lupei, G. Aka and D. Vivien, Optics Communications 204, 399 (2002)
[21] J.B. Gruber, M.E. Hills, T.H. Allik, C.K. Jayasankar, John R. Quagliano and F.S. Richardson, Phys. Rev. B 41, 7999 (1990)
[22] B.M. Walsh, N.P. Barnes, R.L. Hutchenson, R. W. Equall and B. Di Bartolo, J.opt. Soc. Am. B 15, 2794 (1998)
[23] B.M. Walsh, N.P. Barnes, R.L. Hutchenson and R. W. Equall, IEEE Journal of Quantum electronics 37, 1203 (2001)
[24] W.B. Grant, "Lidar for atmospheric and hydrospheric studies" in Tunable Laser Application, F.J. Duarte, Ed. New York: Marcel Dekker 1995, p.241
[25] N.P. Barnes, B.M. Walsh and R.L. Hutchenson, Advanced Solid State Laser 1, 522 (1996)
[26] F.S. Ermeneux, R. W. Equall, R.L. Hutchenson, R.L. Cone, R. Moncorge, N.P. Barnes, H.G. Gallagher and T. P. Han, Advanced Solid State Lasers 26, 242 (1999)
[27] A.A. Kaminskii, "Laser Crystals- Their physics and Properties" Springer, New York 1981
[28] S.Singh, R.G. Smith and L.G. Van Uiter, Phys. Rev B 10, 2566 (1974)
[29] R. C. Powell, "Physics of Solid State Laser Materials" AIP Press Springer, 1998
[30] J.P. Hurrel, S.P.S. Porto, I.F.Chang, S.S. Mitra and R.P. Bauman, Phys. Rev. 173, 851 (1968)

CHAPTER 5

Experimental results: Fe^{3+} doped YAG

5.1 Electron-phonon coupling in Iron doped Yttrium Aluminum Garnet

5.1.1 Experimental setup and growth condition of analyzed samples

Photoluminescence (PL) and excitation of PL (PLE) measurements were carried out at the SUPERLUMI experimental station on the I beamline of the HASYLAB synchrotron laboratories at Desy (Hamburg) by using the pulsed excitation light of the synchrotron radiation (SR). The PLE measurements were performed in the 4-10 eV energy range with 0.3 nm of bandwidth.

Excitation spectra were corrected for the spectral efficiency of the excitation source by using a sodium salicylate standard. The PL signal was dispersed by a 0.5 m Czerny-Turner monochromator and detected in the 1.5–5.0 eV energy range with a charge coupled devices (CCD).

Emission spectral bandwidth was 0.1 nm. PL and PLE spectra were recorded under multi-bunch operation and detected with an integral time window of 192 ns correlated to the SR pulses. A continuous-flow liquid helium cryostat was used to vary the temperature of the sample chamber in the 8-150K range.

Analyzed samples were grown in the growth laboratory Scientific Materials Europe (Italy) by Czochralski method. Pure oxides of Al_2O_3 (99.999%) and Y_2O_3(99.999%) were mixed and pre-sintered under pressure of 140 MPa and processed at 1400° C for 24 hours. Sintered tablets were melt at 1970 °C in an iridium crucible and pulled at 0.8 mm/h with angular velocity $\omega_r = 15$ rpm under Ar atmosphere. Samples were cut along the [111] direction and lapped to optical finish.

5.1.2. Results and discussion

As said before, YAG crystal ($Y_2Al_5O_{12}$) pertains to the space group $Ia3d=O_h^{10}$, with Al^{3+} ions coordinated to the nearest neighbouring oxygens with octahedral and tetrahedral point symmetry. Iron substitutes aluminum in the *a* and *d* sites (point symmetry $G_a=3C_i$ and $G_d=S_4$) with octahedral and tetrahedral oxygen coordination, respectively [1-8].

Since the radius of Fe^{3+} ion is larger than the one of Al^{3+} ion, a distortion of the local lattice structure surrounding the dopant ion (Fe^{3+}) is expected and, effectively, a lattice expansion has been reported [1]. Beside the absorption spectrum modification in the UV (250 nm) and in the visible (407 and 415 nm), emission bands in the near infrared NIR (763 nm) have been related to Fe^{3+} centres [2,6-9].

In addition, Fe^{3+} easily forms covalent bonds with its ligands giving rise to charge transfer transition between the molecular orbital level of the iron ion and the oxygen [1]. Since the crystalline field at the iron ions depends on the local strain, the spectral features related to the dopants can be regarded as a probe of the interaction between the iron ions and the local crystalline field. Static and dynamic strain cause spectral line broadening and shift which are temperature dependent.

Thus, in the case of the Fe^{3+} centres, the interaction between the dopant ions and the host crystal, which is expressed by the electron-phonon coupling (EPC), can be studied by investigating the spectral line peculiarities (shift and broadening) of the NIR emission of iron ion centres. The topic is relevant not only from a fundamental point of view but also technologically, since the energy transfer between iron and aluminum ions in co-doped YAG crystals is related to the EPC of Fe^{3+} centres.

When in the garnet structure the aluminium is totally replaced with iron the Yttrium Iron Garnet (YIG) crystal is formed [10]. YIG is a ferrimagnetic material which is widely used in microwave and optical-communication devices and other applications - mainly due to its magnetic and magneto-optical properties [13-14] like high degree of Faraday effect, high Q factor in microwave frequencies, low absorption in the infrared wavelength region up to 600 nm, and very small line-width in electron spin resonance [13-15].

In the past, different studies have been reported on the coupling parameters of lanthanide ions in garnet crystals [16,17]. These studies were carried out by investigating the thermal dependence of the shape and the spectral position of the zero phonon line, that is by analyzing the quadratic coupling between electrons and phonons.

In Fig. 5.1 the emission spectrum at 10 K of the Fe^{3+} ions in YAG crystal is reported. The excitation wavelength was λ=180 nm, corresponding to the fundamental absorption of the host material [1-6]. The spectrum shows the ZPL centered at 763.0 nm and the phonon repetitions of the ZPL (vibronics) between 770 and 790 nm. The emission properties of Fe^{3+} ions in $Y_3Al_5O_{12}$ are well known and were previously analyzed by Voitukevich *et al.* [6]. These bands derive from the transitions between the fundamental term $^6A_1(S)$ and the term $^4T_1(G)$ of the Fe^{3+} ions.

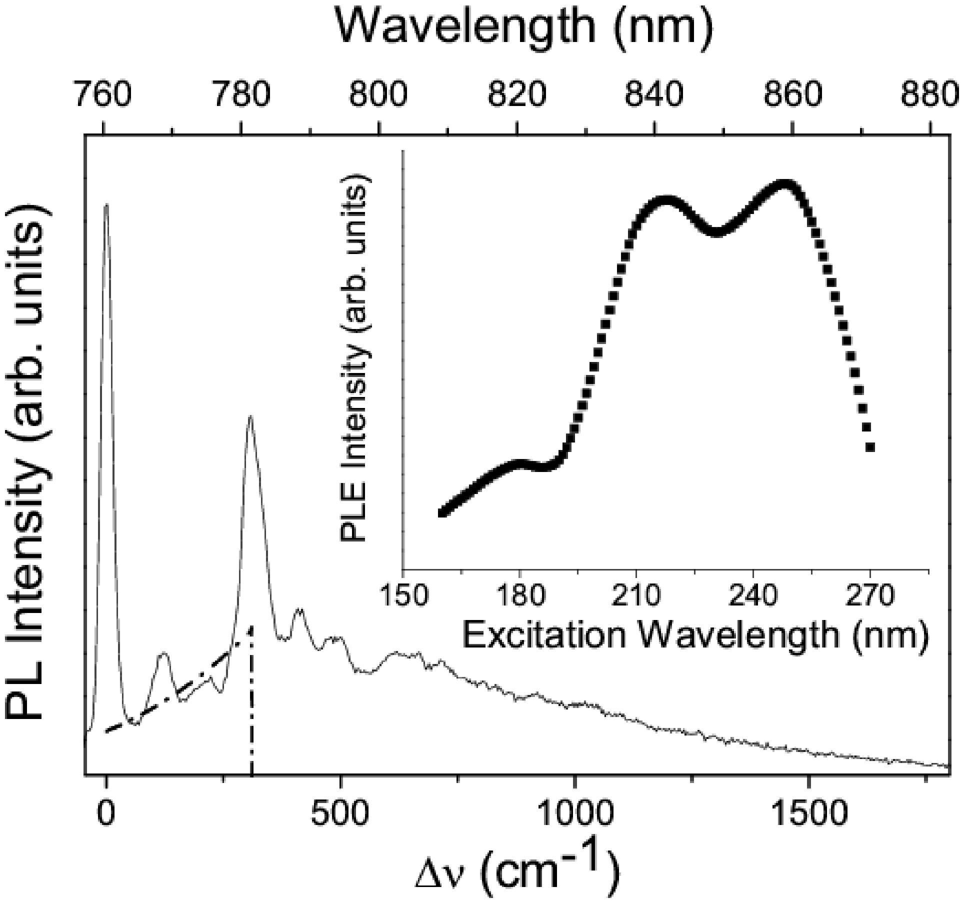

Fig. 5.1. *PL spectrum of ZPL and vibronics at 10 K. The inset reports the PLE spectrum of the ZPL at 10 K. The dash-dotted line shows the fit for the phonon spectrum by using the Debye model.*

The observation of fours fine structure components of the $^4T_1(G)$ emission term in the luminescence spectrum allowed to determine the nature of the crystal field of the environment of the Fe^{3+} ions in the matrix by discriminating the coordination symmetry of the lattice position. The emission features were ascribed to transitions from tetrahedral Fe^{3+} sites [1,6].

The inset of the figure presents the PLE spectrum of the ZPL in the range between 160 and 270 nm. The spectrum shows an intense band in the 230-270 nm region, in good agreements with previous results [9]. This excitation band corresponds to the principal absorption of the Fe^{3+} ions that constitutes the preferential charge transfer channel of the wavelength range around 800 nm. The excitation band at 260 nm is indicated as the convolution of two excitation bands relative to Fe^{3+} ions in tetrahedral and octahedral sites. The peak position of the ZPL is independent of the excitation wavelength in the investigated range.

The PL spectra were recorded at different temperatures in the range between 10 K and 150 K (Fig. 5.2).

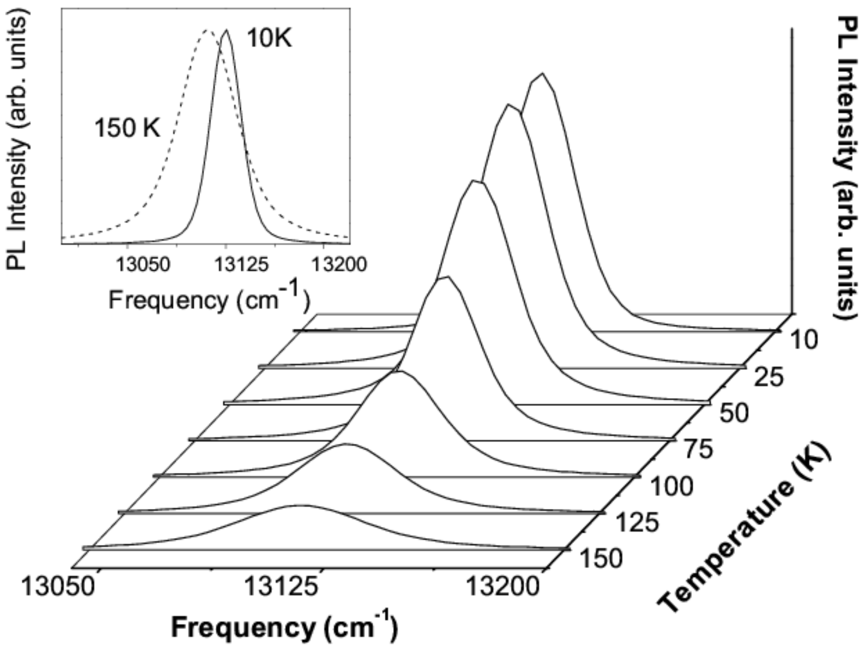

Fig. 5.2. *PL spectra of the ZPL as a function of the temperature in the 10-150 K range. The inset shows the normalized PL spectra at 10 and 150 K.*

As the temperature increases, the pattern of the luminescence spectrum changes sharply and, as previously reported by Voitukevich,[6] it is possible to observe a red shift of the ZPL peak, a substantial broadening of the PL bands and a decrease of the relative intensity of the ZPL band. The inset of Fig. 5.2 shows the normalized PL spectra of the ZPL at 10 and 150 K to better evidence the line shift and broadening. Above the temperature of 150 K the emission bands overlap and the analysis by means of deconvolution is not possible. Thermal quenching of the ZPL can be hypothesized to explain the absence of ZPL signal above 150 K.

At room temperature the spectrum presents a structureless intense broad band peaked at about 810 nm whose shape is asymmetric in the long-wavelength side, with a total width of about 1600 cm^{-1} (here not shown). In addition, the presence of a band centered at 760.6 nm whose relative intensity with respect to the intensity of the ZPL increases as the temperature increases was also reported [6]. Since the $^{4}T_{1}(G)$ levels are very close the one to each other, the integrated area ratio between the ZPL and the band at 760.6 nm is well described by the Boltzmann's law.

Figure 5.3 shows the dependence of the ratio between the integrated area of the ZPL and the whole emission spectrum as a function of temperature. The theoretical curve according to equation (3.15) is also reported.

The best fit result (linear correlation factor R>0.95) gives, for the two adjustable parameters T_D and S, the values of 468 K and 2.05, respectively. This value of the Huang-Rhys factor represents an EPC of medium strength ($1 < S < 6$), where the recombination processes are dominated by transitions to vibrational levels with $\vec{k} > 0$.

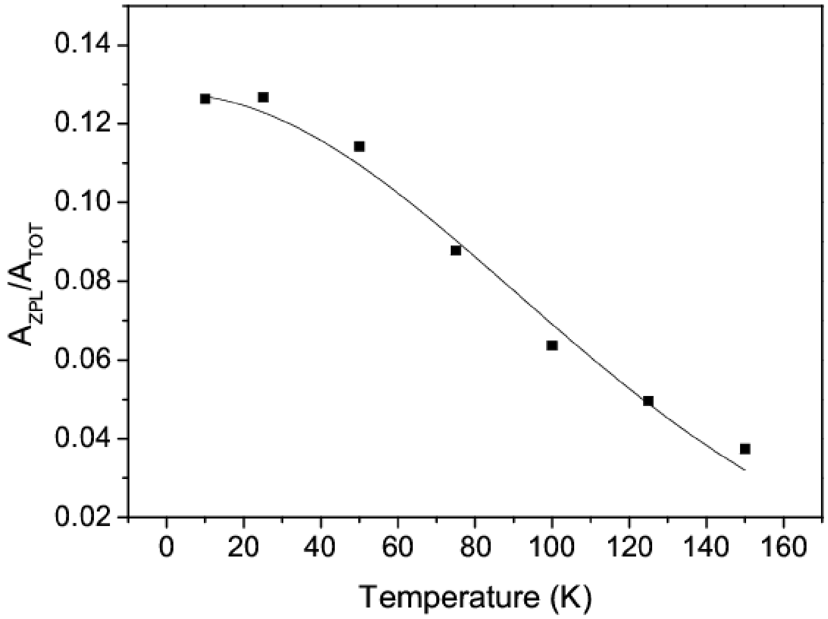

Fig. 5.3. *Dependence of the ratio between the integrated area of the ZPL and the whole emission spectrum as a function of temperature. The solid line reproduces the best fit result according to equation (3.15).*

The ZPL is however still observable. The Debye temperature T_D can be also estimated by means of the Debye model, T_D being a measure for the effective maximum phonon energy. In the Debye model the phonon density increases proportional to ω^2 and then drops to zero at the phonon cut-off frequency ω_{cutoff}. The determination of this parameter can be performed by a graphical method,[14] as illustrated in Fig. 5.1. This method consists in the determination of the cut-off frequency ω_{cutoff}, in the PL spectrum, as corresponding to the maximum of the intensity of the vibronics. At this frequency the phonon density profile drops to zero. The Debye temperature is given by the expression:

$$T_D = \frac{\hbar \omega_{cutoff}}{k_b} \tag{5.1}$$

As illustrated in Fig. 5.1, the phonon density increases to a maximum up to 310 cm^{-1}, in agreement with the Debye model. By assuming this value as the ω_{cutoff} frequency the T_D temperature is estimated as 410 K in reasonable agreement with the value previously reported because the difference between the two values of the Debye temperature is due to the fact that the real density of the phonon states does not fit exactly the Debye model.

In the Fig. 5.4A and 5.4B the spectral line shift and the broadening of the total line width (FWHM) of the ZPL in $Y_3Al_5O_{12}$:Fe^{3+} as a function of the temperature are reported.

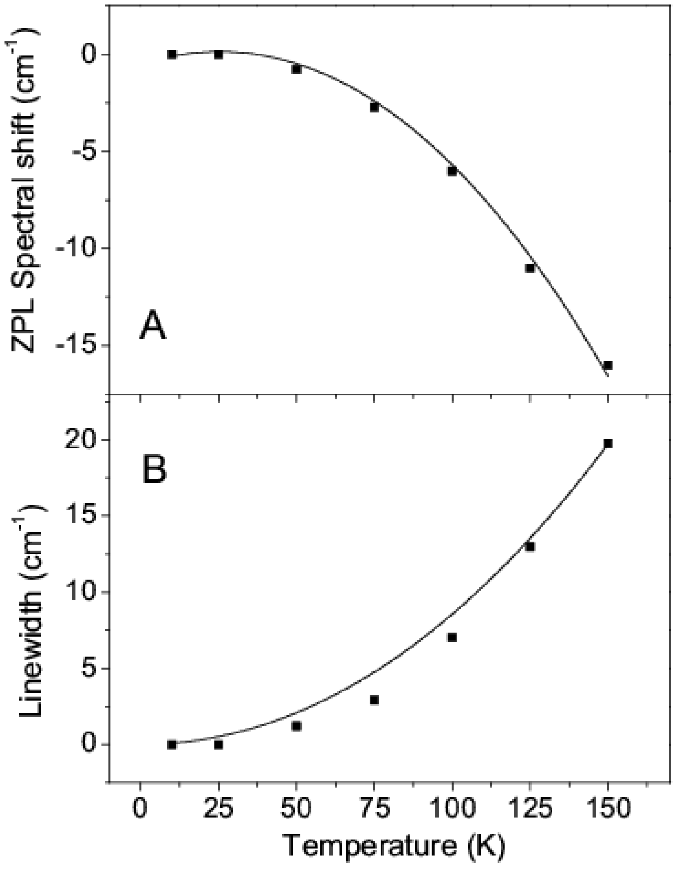

Fig. 5.4. *Line shift (A) and line broadening (B) of the ZPL as a function of the temperature. The solid lines reproduce the best fit results according to equations (5.2) and (5.3) respectively.*

In most studies the contribution of the Orbach process as well as of other minor contributions (such as multi-phonon relaxation) to line shift are neglected [17,24,26]. In addition, if the peak position of the ZPL is independent of excitation energy, the contribution to the shift from localized modes may be neglected [20]. It turns out that the main contributions to the shift of the ZPL originate from quadratic interactions between electrons and acoustic phonons. Hence, one can use the theoretical expression obtained in the Debye model to discuss electron-phonon interactions.

$$E(T) = E(T_{0K}) + \Delta E^R = E(T=0) + \alpha_E \left(\frac{T}{T_D}\right)^4 \int_0^{\frac{T_D}{T}} \frac{x^3}{e^x - 1} dx \qquad (5.2)$$

It has been shown that an increase in temperature causes both blue and red shifts, depending on the material [20,21]. The versus and magnitude of the temperature shift of the ZPL depends on the relation between the shift due to thermal expansion of the crystal lattice and the shift due to electron-phonon interactions at constant volume. The shift of the ZPL due to thermal expansion of the lattice occurs to the blue, while the shift caused by electron-phonon interactions occurs to the red with increasing temperature [20,21].

As the temperature increases, the ZPL shows a red shift of about 16 cm^{-1} between 10 and 150 K (Fig. 5.4A), indicating that the thermal expansion can be reasonably neglected. In other words, when the temperature is well below the Debye temperature, the sample can be regarded as a very “hard” crystal. In this case, the shift due to EPC considerably exceeds the shift caused by the thermal expansion of a crystal, determining the whole experimentally observed line shift.

Figure 5.4A reports the shift of the ZPL as a function of the temperature and the theoretical curve calculated according to equation (5.2). The fit was performed by using the quadratic coupling constant w and the Debye temperature as free parameters (linear correlation factor R>0.99). The results for the two variables are 450 K and -0.85 respectively. The obtained Debye temperature is in good agreement with the values obtained from the linear coupling analysis and from the Debye approximation. As expected, w is larger than –1 [20]. Since a weak quadratic coupling is expressed by a value of w close to zero, the calculated one ($|w| = 0.85$) indicates a relative high quadratic coupling as expected by the relative high shift of the ZPL with temperature when compared to the variation of the ZPL of the Cr^{3+} in the YAG structure in the same temperature range [16].

The study of the ZPL of Cr in YAG crystals reported for the α_E parameter a value of 330 cm^{-1} and a Debye temperature of 550 K. The corresponding w value is -0.6.

Figure 5.4B reports the line broadening of the ZPL in the temperature range between 10 and 150 K. The FWHM was estimated by means of a deconvolution process with Voigt profiles [19,20] and the line width data were fitted according to the theory reported in paragraph 3.3. Actually, Voigt profiles of the emission bands were chosen because of the mixed contribution of homogeneous and inhomogeneous broadening of the spectral lines. It is well known that a physical process that has the same probability of occurrence for all the atoms of the system produces a Lorentzian line shape (homogeneous broadening), while a physical process that has a random distribution of occurrence for each atom produces a Gaussian line shape (inhomogeneous broadening). If both type of broadening processes are present, the line shape is the convolution of Lorentzian and Gaussian contributions represented by a Voigt profile [19,20].

In general, the contribution of direct processes to line broadening is neglected since the evaluation of the electron-phonon strength is not influenced by the incorporation of the direct process in the computation [19]. In addition, in the present case of Fe:YAG, the presence of a large number of crystal field components makes the calculation of the β_{ij} parameter hard to be correctly performed. Moreover, since the radiative relaxation times is of the order of some μs,[5] the radiative relaxation term in equation (3.20) can be neglected.

According to the Heisenberg principle, μs lifetimes broaden the total width less than 10^{-6} cm^{-1}. Therefore, the temperature dependence of the line width of the ZPL can be expressed as

$$\Gamma(T) = \Gamma^{inh} + \Gamma^{R}(T) = \Gamma^{inh} + \alpha_{\Gamma}\left(\frac{T}{T_D}\right)^{7}\int_{0}^{\frac{T_D}{T}} \frac{x^{6}e^{x}}{\left(e^{x}-1\right)^{2}}dx \qquad (5.3)$$

Equation (5.3) was applied to fit the line width of the ZPL as a function of the temperature by assuming the coupling parameters and the Debye temperatures as adjustable parameters. The obtained value for α_{Γ} and for the Debye temperature were 328.9 cm^{-1} and 450 K respectively. Although the theoretical curve reproduces the trend of the experimental points at different temperatures and the fitting parameters are in agreement with the previous results of YAG crystals Cr^{3+} doped,[16] there is not a perfect matching between the experimental data and the proposed model. This fact is clearly showed by deducing the value of the coupling constant w from equation (3.23), w = 0.46, as compared to the value of 0.85 calculated in the line shift fitting procedure.

The disagreement is due to the different approximation used in this analysis, such as the assumption that the inhomogeneous broadening is temperature independent, the neglecting of the direct recombination and the calculation of only the Raman two phonon process as possible dephasing mechanism. Moreover, the EPC is not the same for all phonon modes and can be in principle different for phonons contributing to line broadening processes compared to those contributing to line shifting processes. Except for this discrepancy, the perturbation approach described here has been very successful in providing an understanding of the thermal properties of spectral lines of ions in solids [26].

A summary of the results obtained in this work shows that the evaluated Huang-Rhys parameter is 2.05 and the quadratic coupling factor is $|w| = 0.85$. The estimated Debye temperature is about 450 K.

A final comments pertains to the fact that the above expressions for the spectral line shift and line broadening, equations (5.2) and (5.3) respectively, are calculated by assuming the Debye model. One should bear in mind that the actual phonon distribution is far from the model but the thermal dependence is often well described by a single characteristic temperature which can be interpreted as an effective Debye temperature which may not coincide with the value extracted from heat measurements because not the whole set of phonons is coupled with the ions.

The performed study shows a relatively easy method to study the EPC strength in Fe^{3+} doped YAG crystals and the model can be extended to other materials. Although a more rigorous non perturbative method can be developed to explain the temperature dependences of spectral line widths and position, the simpler mathematics of the described perturbation approach provides a better insight into the physical processes that are taking place.

References

[1] Die Dong, Kuang Xiao-Yu, Guo Jian-Jun, Wang Hui, and Zhou Kang-Wei Phys. Rev. B 72, 073101 (2005).

[2] S.R. Rotman, C.Warde, H.L. Tuller and J. Haggerty J. Appl. Phys 66 3207 (1989).

[3] Y.F. Chen, K.T. Wu, Y.D. Yao, C.H. Peng, K.L. You and W.S. Tse Microelectr. Engin. 81, 329 (2005).

[4] M.V. Korzhik, M.G. Livshits, B.I. Minkov, and V.B. Pavlenko Sov J. Quantum. Electron 22, 24 (1992).

[5] M.V. Korzhik, M.G. Livshits, M. L. Meilman, B.I. Minkov, and V.B. Pavlenko Opt. Spectrosc. 70, 471 (1991).

[6] Yu. A. Voitukevich, M. V. Korzhik, V.V. Kuzmin, M.G. Livshits, and M.L. Meilman Opt. Spectrosc. 63, 810 (1987).

[7] M.V. Korzhik, M.G. Livshits, Kh, S. Bagdasarov, A.M. Kevorkov, T.A. Melkonyan, and M.L. Meilman Sov J. Quantum. Electron 19, 344 (1989).

[8] J. P. Hurrell, P.S. Porto, I.F. ChNG, s.s. Mitra and R.P. Bauman Phys Rev B 173 851 (1968).

[9] M.L. Meil'man, M.V. Korzhik V.V. Kuzmin, M.G. Livshits, Kh, S. Bagdasarov, and A.M. Kevorkov, Sov. Phys. Dokl. 29(1), 61 (1984).

[10] G.B. Scott, D.E. Lacklison, and J.L. Page Phys. Rev. B 10, 971 (1974).

[11] R. Urban, A. Putilin, P. E. Wigen, S.-H. Liou, M. C. Cross, P. C. Hammel, and M. L. Roukes Phys. Rev. B 73, 212410 (2006).

[12] A. S. Tatarenko, G. Srinivasan, and M. I. Bichurin Appl. Phys. Lett. 88, 183507 (2006).

[13] Y. V. Khivintsev, Bijoy K. Kuanr, Ian Harward, R. E. Camley, and Z. Celinski J. Appl. Phys. 99, 08P512 (2006).

[14] G. A. Melkov, V. I. Vasyuchka, Yu. V. Kobljanskyj, and A. N. Slavin Phys. Rev. B 70, 224407 (2004).

[15] A.A. Semenov, S.F. Karmanenko, B.A. Kalinikos, G. Srinivasan, A.N. Slavin, and J.V. Mantese Electron. Lett. 42, 641 (2006).

[16] A.P. Vink, A. Meijerink, J. of Phys. and Chem. of solids 61, 1717 (2000).

[17] A. Ellens, H. Andres, A. Meijerink, and G. Blasse Phys, Rev. B 55, 173 (1997).

[18] Baldassarre Di Bartolo, *Optical Interactions in Solids* (Wiley, New York,1968), chap. 15.

[19] Richard C. Powell, *Physics of Solid-State Laser Materials* (Springer-Verlag, New York, inc. 1998), chap. 4-5.

[20] H. Wang, F.D. Medina, D.D. Liu, and Y.D. Zhous, J. Phys.: Condens. Matter 6, 5373 (1994).

[21] J.L. Skinner, and D. Hsu Adv. Chem. Phys. 65, 1 (1986).

[22] G.P. Srivastava The Physics of Phonons (Adam Hilger, IOP, New York, 1990), chap. 2-7.

[23] D. Hsu, and J.L. Skinner J. Chem. Phys. 81, 1604 (1984).

[24] M.G. Beghi, C.E. Bottani, and V. Russo J. Appl. Phys. 87, 1769 (2000).

[25] T.E. Jenkins J. Phys. C: Solid State Physics 19, 1065 (1986).

[26] D.E. McCumber, and M.D. Sturge J. Appl. Phys. 34, 1682 (1963).

[27] J.L. Skinner J. Chem. Phys. 36, 322 (1988).

Conclusions

This PhD thesis is concerned with the optical and structural characterization of crystalline oxides for laser application; the aim was to enhances efficiency and tunability of active media, and the experimentation of new materials able to meet specific purposes.

In collaboration with Scientific Materials Europe, we studied two different materials with garnet structure: the mixed structure $Y_3Sc_2Ga_3O_{12}$ (YSGG) - $Y_3Al_5O_{12}$ (YAG) doped with Neodymium, and yttrium aluminum garnet ($Y_3Al_5O_{12}$ -YAG) doped with Fe^{3+} ions.

Different spectroscopic techniques were utilized in order to characterize the above mentioned materials and to optimize the growing processes.

By means of Raman spectroscopy the analysis of the vibrational properties of Yttrium Aluminum Garnet (YAG), Yttrium Scandium Gallium Garnet (YSGG) and mixed $YAG_x/YSGG_{1-x}$ garnets ($0<x<1$) was carried out.

By comparison with the vibrational spectrum of the YAG structure, the attribution of the Raman modes of the YSGG is proposed. The formation of mixed crystals was verified by analyzing the spectra within the isolated polyhedra framework. The Raman spectra of the mixed garnets do not show the presence of new vibrational bands: the mixed structure vibrations show one-mode behavior indicating the presence of truly solid state solution

In the approximation of free polyhedra, the position of the vibration frequencies of the A_{1g} tetrahedron breathing mode as a function of the relative concentration of the garnets was investigated by modeling the interaction potential as a linear combination of the contribution due to the pure structures. The proposed analysis allows to verify both the quality of the grown crystal and to asses the relative concentration of the garnets. The peak position of the A_{1g} frequency can be analyzed to assess the effective mixing of the two garnets and the relative concentration of the grown crystal. Raman spectroscopy is, therefore, a powerful diagnostic tool to check the quality of the grown crystal:

The photoluminescence properties of Nd doped YAG and YSGG mixed structures are also reported. As the relative concentration of the YSGG increases a blue shift of the R_1-Z_5 and R_2-Z_5 transitions is observed. The reported data were successfully explained by confirming a mixed garnet structure where the two crystalline phases are mixed at the unit cell level. We proposed an analytical model on the Nd^{3+} emitting wavelengths based upon the modification induced on the local crystalline field by the substitution of the Al cations of YAG structure with the Sc and Ga cations of the YSGG. The model successfully predicts the observed effect of the compositional tuning. In addition, the proposed model does not depend on the mixed garnet of choice but could be exported to similar garnet structure.

In order to enhance the efficiency of solid state laser medium, like Nd:YAG, we studied the electron-phonon coupling in Iron doped Yttrium Aluminum Garnet crystal. By analyzing the experimental data in the theoretical framework of linear and quadratic coupling the line shift and line broadening of the Zero Phonon Line of iron centers as a function of the temperature in the 10-150 K is qualitatively and quantitatively explained.

The applied model, based on a perturbative approach, indicates a linear coupling of medium strength and a strong quadratic coupling, providing an understanding of the thermal properties of spectral lines of ions in solids.

This work is a basis for a full understanding of the role of Iron ions as sensitizer element in Nd doped garnet crystals.

Synergic efforts between Scientific Materials Europe and the University of Cagliari, have shown how the study of the basic optical properties of crystalline oxides allows to improve industrial processes and to develop innovative materials.

Complementary research activities

During the three years of the PhD course, further studies were developed within the research activities of the Optical Spectroscopy Group and the Laboratorio di Microscopie e Nanoscopie (LIMINA).

Regarding the research activities of the Optical Spectroscopy Group, I have been involved in a research project about wide gap compounds and dielectrics. In particular fluorescence properties of Alkaline Earth Thiogallate doped with Ce, Pr and Eu were studied by means of non conventional spectroscopic techniques. Moreover, photoluminescence measurements on porous Silica samples were carried out with the synchrotron radiation as excitation source. These measurements were performed during two experimental sessions at SUPERLUMI station of the DESY laboratories in Hamburg (Germany).

In addition, a new research branch related to oxide crystals was developed. This work was carried out in collaboration with the Scientific Materials Europe where an internship about Czochralski growth technique was spent. It leaded to the optical characterization of LYSO ($Lu_{1.8}Y_{0.2}SiO_5$) which is a new attractive material for scintillation applications.

Within the research activities of LIMINA I have been involved in the installation and management of Environmental Scanning Electron Microscopy (ESEM) facility. This work also lead to the development of analytical techniques by means of Scanning Electron Microscopy (SEM).

List of Publications

"Electron-phonon coupling in Iron doped Yttrium Aluminum Garnet" A. Anedda, C.M. Carbonaro, D. Chiriu, R. Corpino, M. Marceddu, P.C. Ricci - Physical Review B Vol. 74, 245108 (2006)

"*Vibrational Properties of mixed $(Y_3Al_5O_{12})_x$-$(Y_3Sc_2Ga_3O_{12})_{1-x}$ crystals"* D.Chiriu, P.C. Ricci, C.M. Carbonaro, A. Anedda, M. Aburish-Hmidat, A. Grosu, PG. Lorrai and E. Fortin – Journal of Applied Physics Vol. 100 (3), 33101 (2006) in collaboration with Scientific Materials Europe.

"*Compositional tuning of photoluminescence properties in Nd-doped YAG-YSGG structures"* A. Anedda, C.M. Carbonaro, D. Chiriu, P.C. Ricci , M. Aburish-Hmidat, M. Guerini, P.G. Lorrai and E. Fortin – IEEE Journal of Quantum Electronics 42 (6), 563 (2006) in collaboration with Scientific Materials Europe.

"Photoluminescence of Ce and Pr codoped Calcium Thiogallate" A. Anedda, C.M. Carbonaro, D. Chiriu, R. Corpino, M. Marceddu, P.C. Ricci , A.N. Georgobiani, B.G. Tagiev, O.B. Tagiev, S.A. Abushev and I. M. Tiginyanu – Physica Status Solidi (C) – Vol. 3(8), 2717 (2006)

"Donor-Acceptor pairs and excitons recombinations in $AgGaS_2$" M. Marceddu, A. Anedda, C.M. Carbonaro, D. Chiriu, R. Corpino and P.C. Ricci - Applied Surface Science – Vol. 253, 300 (2006)

"*Photo-electrochemical formation of porous GaP*", P.C. Ricci, A. Anedda, C.M. Carbonaro, D. Chiriu, F. Clemente, R. Corpino - Physica Status Solidi (C) 9, 3365 (2005).